bioRxiv preprint doi: https://doi.org/10.1101/2020.10.26.353656; this version posted October 26, 2020. The copyright holder for this preprint (which was not certified by peer review) is the author/funder. All rights reserved. No reuse allowed without permission.

ZeBraInspector, a whole organism screening platform enabling volumetric analysis of zebrafish brain white matter

Sylvain Lempereur[a,b,*], Elodie Machado[b], Fabrice Licata[b], Lilian Buzer[a], Isabelle Robineau[b], Julien Hémon[b], Payel Banerjee[b], Noémie De Crozé[c], Marc Léonard[c], Pierre Affaticati[b], Arnim Jenett[b], Hugues Talbot[a,d], Jean-Stéphane Joly[b, *]

AFFILIATION

a. LIGM, Univ Gustave Eiffel, CNRS, ESIEE Paris, F-77454 Marne-la-Vallée, France
b. Tefor Paris-Saclay, UMS 2010, CNRS, INRAE, Université Paris-Saclay, Gif sur Yvette, France
c. L'Oréal, Research & Innovation, Aulnay sous Bois, France
d. Université Paris-Saclay, Centrale Supélec, INRIA, 91190, Gif-sur-Yvette, France

* Corresponding authors.
E-mail addresses : sylv.lempereur@gmail.com (S. Lempereur); jean-stephane.joly@cnrs.fr (J.-S. Joly)

websites:

- TEFOR Paris-Saclay – Research and Development for the Tefor Infrastructure
- ZeBraInspector – Tefor
- ZeBraInspector – Gitlab repository

Keywords: fish, tissue clearing, confocal imaging, morphometry, computer vision, teratology

Acknowledgements

We wish to thank Marie-Elise Schwartz and Julien Hémon for skillful fish rearing. Jean-Pierre Levraud is acknowledged for sharing pictures of two transgenic lines. Koji Ando is thanked for the kdlr-DsRED line. We acknowledge Elodie De Job and Laurie Rivière for their expert technical contribution to the development of our tissue-clearing procedures, Anna Renoux for the genotyping of *wdr*12 fish, Maxence Frétaud, Christelle Langevin and Violette Thermes for their contributions to protocol development by helpful discussions in the frame of the TEFOR phenotyping group. Lionel Moreira and Vincent Jourdain are acknowledged for their contribution to the TEFOR portfolio webpage. Giovanni Cherchia and Barbara Rizzi are also thanked for their advice concerning algorithm developments. Kleio Petratou, Ali Kiai and Stefan Schulte-Merker are thanked for their comments on the ZBI software. Johanna Djian-Zaouche is thanked for discussion and support. This work was supported by ANR-TEFOR-"Investissement d'avenir" (ANR-II-INBS-0014), ANR FINEST (ANR- 2011-SVSE2-001-01), ANR Fish-RNAvax (ANR-16-CE20-0002-01), ANR FEATS (ANR-19 -CE34-0005-05) and institutional supports from CNRS and INRAE. We warmly thank the Leducq foundation for its RETP grant and for constant support, which was central for the development of the ZBI platform. SL received a PhD grant from Université Paris-Est.

bioRxiv preprint doi: https://doi.org/10.1101/2020.10.26.353656; this version posted October 26, 2020. The copyright holder for this preprint (which was not certified by peer review) is the author/funder. All rights reserved. No reuse allowed without permission.

SUMMARY

In recent years, zebrafish have become well established for the study of fundamental biology, toxicology and drug discovery. Here we propose fast, standardized protocols for high-throughput and high-content 3D imaging of 5dpf zebrafish EE using a confocal laser scanning microscope. Using a lipophilic fluorescent dye, we generated a reference labeling in cleared fish. We developed a mounting method based on 3D-printed stamps used to create a grid of wells in an agarose cast. We demonstrate that the quality and homogeneity of the fluorescence signal allows an unequivocal segmentation of the whole specimen and the white matter. From there, we built an automated image registration and analysis pipeline for the volumetric analysis of morphological defects. The platform, termed ZeBraInspector, is focused on the analysis of the shape of the whole EE or the white-matter of the central nervous system. A user-friendly software to visualize at large scale registered and segmented 3D images can be downloaded from https://tefor.net/portfolio/zebrainspector. We finally provide two examples of application: the characterization of a phenotype associated with a neuro-developmental mutation, and the defects caused by treatments with a toxic anti-cancer compound. ZeBraInspector can be adapted to a wide variety of high-content analyses.

bioRxiv preprint doi: https://doi.org/10.1101/2020.10.26.353656; this version posted October 26, 2020. The copyright holder for this preprint (which was not certified by peer review) is the author/funder. All rights reserved. No reuse allowed without permission.

Introduction

With the increasing demand of tests on toxicity and biocompatibility of active chemical components (Buitrago Santanilla et al., 2015; Cernak et al., 2017)), need for high-content screens (HCS) based on high-content imaging (HCI) and high-content analysis (HCA) have become extremely diversified. A variety of screening methods evolved from simple 2D methods (Beaumont et al., 2015; Staal et al., 2018) to 2D+time (Cornet et al., 2017), high-throughput-techniques in 2D (Jarque et al., 2018) and pseudo-3D (optical projection tomography (OPT) (Xiaoqin Tang et al., 2016). Sophisticated automates were developed, such as those that deliver zebrafish EE in capillaries (vertebrate automated screening technology (VAST) (Early et al., 2018; Guo et al., 2017; Pulak, 2016)

For HCS, light-sheet microscopes are fast but limited in the numbers of mounted samples per batch. Confocal microscopy allows high-throughput imaging (HTI) but is limited when deeper structures need to be imaged (Bruneel and Witten, 2015), due to light diffraction on the interface of adjacent tissue-components with varying refractive indexes. However, tissue clearing methods have recently progressed to allow deeper imaging including in zebrafish (Affaticati et al., 2017; Susaki et al., 2014). One of the key steps for rendering tissues optically clear is the matching of the refractive index (RI) of the samples to that of the mounting medium.

Zebrafish, a vertebrate model has high biological and physiological, and body plan similarity to humans (Planchart et al., 2016; Roper and Tanguay, 2018) with reduced ethical concerns. Indeed, eleuthero-embryos (EE), EE which do not feed, fall outside of the european directive on animal experimentation (Halder et al., 2010). Advantages of this model for HTS are low breeding costs and high fecundity. Due to their small size, tests can be performed on EE in high-throughput settings using 96-well plates.

Here we develop the ZeBraInspector (ZBI) platform using fast labeling and tissue clearing protocols, dedicated 3D-printed mounting stamps and a fast automated confocal laser scanning microscope (CLSM).

The ZeBraInspector (ZBI) software (https://tefor.net/portfolio/zebrainspector) can be used for the smooth and fast observations of a large number of registered samples. A major advantage of this software is indeed that, thanks to sophisticated algorithms, an imprecise mounting orientation around the antero-posterior axis of the fish is tolerated to a certain degree. This makes the mounting step much faster than when accurate orientations are needed.

Using lipophilic dyes (such as DiI or DiO), we strongly label brain white matter and also highlight whole EE and then perform the automatic detections and segmentations of labeled domains. A user-friendly interface is proposed to validate segmentations and select segmented samples for a volumetric analysis.

To exemplify the usefulness of the ZBI platform for various applications, we focus on a mutant having potential microcephaly and on a long-prescribed chemotherapeutic drug, being an environmental contaminant affecting aquatic animals and having potential teratogenic effects in humans.

bioRxiv preprint doi: https://doi.org/10.1101/2020.10.26.353656; this version posted October 26, 2020. The copyright holder for this preprint (which was not certified by peer review) is the author/funder. All rights reserved. No reuse allowed without permission.

Materials and Methods

Zebrafish housing and husbandry

Fish were reared at a density of five adults per liter under controlled conditions according to european recommendations for zebrafish housing and care (Aleström et al., 2019). Environmental parameters were as follows : photoperiod = 14 h/10 h light/dark, temperature = 26.5 ± 1 °C, pH = 7.8 ± 0.1; conductivity = 240 ± 30 µS/cm, NH4+ = 0 mg/L, NO2- = 0 mg/L, NO3-< 50 mg/L. Fish were fed on rotifers (*Brachionus plicatilis*, > 500/fish/day) for the first two weeks of feeding, and then with brine shrimps (*Artemia nauplii*, ~250/fish/day) and dry food (Skretting, Gemma Micro, to apparent satiation, two times/day). Lines used in these studies were AB (from European Zebrafish Resource Center, Germany), casper (from Zon Lab, Harvard University, USA), *Tg(kdrl:DsRed)* (obtained from Betsholtz lab), *Tg(fli:GFP)* and *wdr12*^{hi3120Tg} mutant line (from Zebrafish International Resource Centre, Eugene, Oregon). All procedures were performed in accordance with European Union Directive 2011/63/EU and were approved by the local ethics committee (no. 59 CEEA).

Four fast staining protocols for the lipophilic carbocyanine dyes (DiI, DiO, DiD, DiR), fluorescent proteins, and optionally various antibody stainings

Single dye staining (Fig. 0A)

Five days post-fertilization (dpf), EE were euthanized and immersed overnight in fixative solution (4% formaldehyde in 1X phosphate buffer saline PBS, 0.1% Tween 20 (PBST) at 4°C. They were processed immediately or stored up to several weeks at 4°C in PBST containing 0.5% formaldehyde and 0.05% sodium azide. They were thoroughly washed in PBST for two days and incubated in 0.5X saline sodium citrate buffer (SSC) with 0.1% Tween 20 for 1h at RT. Melanocytes were then bleached in a fresh depigmentation solution (0.5X SSC, 5% formamide, 3% H2O2) for 1h at RT and subsequently the samples were washed overnight in PBST. After a minimum of 5h incubation in blocking solution (10% normal goat serum, 10% DMSO, 5% PBS-glycine, 0.5% Triton X-100, 0.1% deoxycholate, 0.1% NP40 and 0.1% saponin in PBST) at room temperature, samples were quickly rinsed in PBST and labeled for three days with 1 µg/ml of lipophilic dye (DiI, DiO, DiA, DiD or DiR, L7781, ThermoFisher) in labeling solution (1X PBST containing 2% normal goat serum, 20% DMSO, 0.05% sodium azide, 0.2% Triton X-100, 10µg/ml heparin and 0.1% saponin) at RT with gentle agitation. Samples were then subjected to refractive index (RI) matching and mounting.

Dye staining preserving native fluorescent proteins (Fig. 0B-C)

Five days post-fertilization (dpf), EE were euthanized and immersed overnight at 4°C or 2 hours at room temperature in fixative solution (4% formaldehyde in 1X phosphate buffer saline PBS, 0.1% Tween 20 (PBST). They were processed immediately or stored up to several weeks at 4°C in PBST containing 0.5% formaldehyde and 0.05% sodium azide. They were thoroughly washed in PBST for two days and immersed for a minimum of 5h in blocking solution (10% normal goat serum, 10% DMSO, 5% PBS-glycine, 0.5% Triton X-100, 0.1% deoxycholate, 0.1% NP40 and 0.1% saponin in PBST) at room temperature. Samples were quickly rinsed in PBST and labeled for three days with 1 µg/ml of lipophilic dye (DiI, DiO, DiA, DiD or DiR, L7781, ThermoFisher) in labeling solution (1X PBST containing 2% normal goat serum, 20% DMSO, 0.05% sodium azide, 0.2% Triton X-100, 10µg/ml

bioRxiv preprint doi: https://doi.org/10.1101/2020.10.26.353656; this version posted October 26, 2020. The copyright holder for this preprint (which was not certified by peer review) is the author/funder. All rights reserved. No reuse allowed without permission.

heparin and 0.1% saponin) at RT with gentle agitation. Samples were then subjected to refractive index (RI) matching and mounting.

Dye staining coupled with immuno-detections (Fig.0D-H)

To combine whole-mount lipophilic dye staining with immunodetection, we proceeded as follows. Five days post-fertilization (dpf), EE were euthanized and immersed overnight in fixative solution (4% formaldehyde in 1X phosphate buffer saline PBS, 0.1% Tween 20 (PBST) at 4°C. They were processed immediately or stored up to several weeks at 4°C in PBST containing 0.5% formaldehyde and 0.05% sodium azide. They were thoroughly washed in PBST for two days and incubated in 0.5X saline sodium citrate buffer (SSC) with 0.1% Tween 20 for 1h at RT. Melanocytes were then bleached in a fresh depigmentation solution (0.5X SSC, 5% formamide, 3% H2O2) for 1h at RT and subsequently samples were washed overnight in PBST. After a minimum of 5h in blocking solution (10% normal goat serum, 10% DMSO, 5% PBS-glycine, 0.5% Triton X-100, 0.1% deoxycholate, 0.1% NP40 and 0.1% saponin in PBST) at room temperature, samples were briefly rinsed in PBST and incubated with primary antibodies in staining solution (1X PBST buffer containing 2% NGS, 20% DMSO, 0.05% sodium azide, 0.2% Triton-X100, 10µg/mL heparin and 0.1% saponin) under gentle agitation for three days at 37°C. Samples were washed for at least 1h in PBST at RT and incubated with secondary antibodies for three days at 37°C in the dark, with gentle agitation in staining solution without saponin. Samples were washed in PBST for at least 2h and stained for three days with 1 µg/ml of lipophilic dye (DiI, DiO, DiA, DiD or DiR, L7781, ThermoFisher) in staining solution without saponin at RT with gentle agitation. Samples were then subjected to refractive index (RI) matching and mounting.

5-FU and *wdr12* samples were immunolabeled with anti HuC/D (not shown) (ab210554, abcam, used at 1:600). Anti-GFP (GFP-1020, Avès labs) and anti-DsRed (632496, Ozyme) were used at 1:400-1:600 dilutions. Secondary antibodies were Alexa fluor 555-conjugated goat anti-rabbit (A-21428, ThermoFisher, used at 1:600), Alexa fluor 488-conjugated goat anti-chicken (A-11039, ThermoFisher, used at 1:600).

bioRxiv preprint doi: https://doi.org/10.1101/2020.10.26.353656; this version posted October 26, 2020. The copyright holder for this preprint (which was not certified by peer review) is the author/funder. All rights reserved. No reuse allowed without permission.

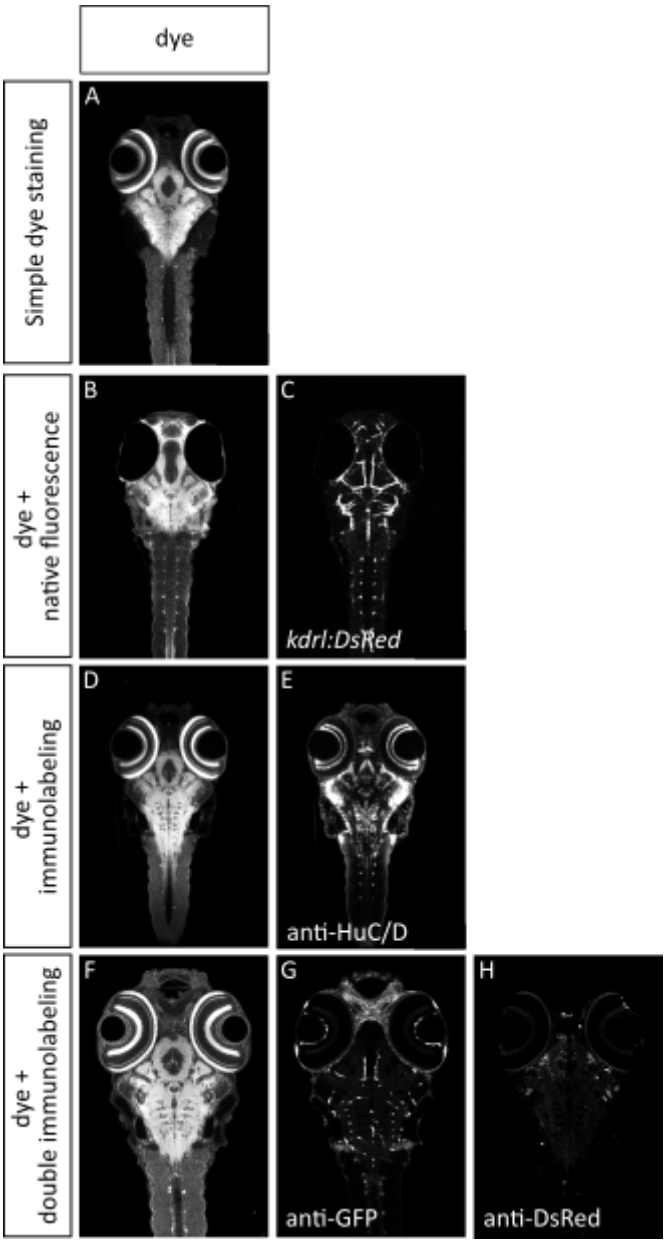

Fig. 0: Four examples of fast staining protocols compatible with the ZeBraInspector (ZBI) platform

(A) Confocal horizontal optical section of a 5dpf zebrafish after DiO staining. (B-C) zFaCT labeling protocol is compatible with native fluorescence imaging. A 5dpf EE from *Tg(kdrl:DsRed);casper* transgenic reporter of endothelial cells of the blood vasculature was counterstained with DiO. (B) Confocal horizontal optical section of the DiO channel. (C) The same optical section showing DsRed fluorescence. (D-E) zFaCT labeling protocol allows whole-mount immunolabeling. A 5dpf EE was labeled with an anti-HuC/D antibody to label neurons and counterstained with DiO. DiO and anti-HuC/D patterns from the same horizontal optical section are shown in D and E respectively. (F-H) 3 channel imaging was performed on immunolabeled 5dpf EE from *Tg(fli:GFP)* transgenic line injected with SINV-mCherry/2A at day 3 . DiD, GFP (anti-GFP antibody) and mCherry (anti-DsRed antibody) fluorescent patterns from the same horizontal optical section are shown in F, G and H respectively.

bioRxiv preprint doi: https://doi.org/10.1101/2020.10.26.353656; this version posted October 26, 2020. The copyright holder for this preprint (which was not certified by peer review) is the author/funder. All rights reserved. No reuse allowed without permission.

Mounting and refractive index (RI) matching

We used a RI matching medium (50% sucrose (w/v), 20% nicotinamide (w/v), 10% triethanolamine (w/v) and 0.1% TritonX-100 (v/v)), hereinafter referred to as MD+, modified from the CUBIC-2 (Susaki et al., 2015) solution. Urea was replaced by nicotinamide, which has strong optical clearing ability (Tainaka et al., 2018). RI of MD+ was adjusted with water to 1.457. Dye stained samples were first incubated in 0,5X MD+ (50% (vol/vol) in dH_2O) for at least two hours and then transferred to MD+ solution. Mounting plates were coated with hot agarose/MD+ (1.5% and 2% agarose solubilized in MD+ for standard 60mm petri dishes and single-well plates, respectively) and appropriate stamps positioned rapidly. Stamps were removed after agarose hardened. Using a paintbrush, fish were carefully mounted in the resulting niches, then encased in small drops of phytagel/MD+ (1% phytagel solubilized in MD+) to stabilize them during subsequent steps. The mounting plates were filled with MD+ and the RI was checked several hours later. Plates whose RI matched 1.457 were imaged, if not, MD+ solution was renewed as often as necessary to reach this value.

3D printed mounting molds

Initially prototyped in sketchup (Trimble Inc, USA), we soon switched the development of the stamps to the open source CAD software Openscad (Kintel and Wolf, 2020) because the small modifications needed during the development- and test-phase are easier and more reliable to implement on a numeric model than on a graphic one.

The resulting files are hosted on gitlab:

stamp for 12 samples: https://gitlab.com/sylv.lempereur/tcfmodels/-/blob/master/petri_whole_5dpf_dr.scad

stamp for 48 samples: https://gitlab.com/sylv.lempereur/tcfmodels/-/blob/master/halfPlate_whole_5dpf_dr.scad

stamp for 96 samples: https://gitlab.com/sylv.lempereur/tcfmodels/-/blob/master/plate_whole_5dpf_dr.scad

handle for all stamps: https://gitlab.com/sylv.lempereur/tcfmodels/-/blob/master/handle.scad

These files were sliced with Cura 4 (Ultimaker, Netherlands) and printed in polylactic acid (PLA) on a standard Ultimaker 2^+ (Ultimaker, Netherlands) using a 0.25 mm nozzle. For achieving the highest resolution and fidelity in the ridges which are forming the small niches for the EE, we print these stamps upright, standing on the straight edge of the long side. All stamps are handled with one to two default handles, which are printed in bulk separately and are affixed to the stamp with superGlue (cyanoacrylate, CA).

Imaging plates

For small batches (up to twelve EE), we used standard 60mm petri dishes (Greiner Bio One International, catalog number: 628160) with the twelve sample stamp. Bigger batches were mounted using the stamps for 48 or 96 specimens in Single-Well Plates (ThermoFisher, #140156).

bioRxiv preprint doi: https://doi.org/10.1101/2020.10.26.353656; this version posted October 26, 2020. The copyright holder for this preprint (which was not certified by peer review) is the author/funder. All rights reserved. No reuse allowed without permission.

These provide ample space for the microscope's objective and have the outside dimensions of a standard 96-well plate (Fig.3C). This permits mounting of the dish on the microscope's stage using standard hardware.

Confocal imaging

Due to the high sample number needed, our HCS imaging requires a high-speed and efficient image acquisition setup. For this purpose, we designed a setup based on a NIKON A1R HD microscope combined with a long range objective piezo scanner (2mm), a fast motorized stage and a low magnification objective (10x, 0.5NA).

This microscope incorporates a high-definition resonant scanner, a band-pass (BP) filtered four-channel detector unit equipped with two high-sensitivity GaAsP detectors (BP 525/50 & 595/50) and two photomultiplier tubes (PMT) (BP 450/50 & 700/75). The laser unit is equipped with four laser diodes (405 nm, 488 nm, 561 nm, 640 nm. Power > 15mW) which are switched by an acousto-optic-tunable filter (AOTF). To allow high-speed plate displacement in the X/Y plane a fast motorized stage Prior H101P2 was chosen.

In order to optimise the field of view, we combined the A1R Nikon with large field of view (18mm) with a CFI Plan Apo 10XC Glyc (0.5NA) immersion objective (Nikon) to allow acquisition of images (tiles) with X-Y sizes of 1200 x 1200 µm, such that the 5dpf fish (diameter: 800 µm length: 4mm) could be captured entirely with only five tiles. Furthermore, this setup provides a working distance of 5.5mm and correction for a wide range of refractive index, from 1.33 to 1.51.

To ensure rapid image acquisition in the z-plane, we use a fast piezo objective scanner (PIFOC, Physik Instrumente, Karlsruhe, Germany) allowing high speed acquisitions over 2mm in Z.

Filename based data management for HCA

Maintaining flexibility in the choice of analytic tools and accessibility to a wide variety of users, we developed a data management system based on structured file names. Since it is independent of a centralized tracking database the organization of the data can be upheld even after export to a different environment, e.g. the lab of a collaborateur or user of our service unit.

The structured file name constitutes the 'globally unique identifier' (GUID) for each sample and is, due to its consistent structure, as easily readable by humans as it is to machines.

For images, it consists of a combination of condensed composite IDs, which are separated by underscores: scanID_specimenID_experiment-descriptor_data-descriptor. Each of these again can be broken down into less complex descriptors:

- The scanID is the acquisition date in the format yymmdd (year, month, day; two digits each, zero-padded) followed by the initial of the person who acquired this image (capitalized) and an alphabetic counter (a-z) counting the scans performed by this person on this day. Having the scanID in this form and at this position forces the files in chronological order, which facilitates finding (potential related) files of the same session in a system file manager (explorer, finder, nautilus).

bioRxiv preprint doi: https://doi.org/10.1101/2020.10.26.353656; this version posted October 26, 2020. The copyright holder for this preprint (which was not certified by peer review) is the author/funder. All rights reserved. No reuse allowed without permission.

- The specimenID consists of the experimentID, which identifies a batch of samples of a project, and an alphabetical counter, which individualizes for each specimen.

- The experiment-descriptor contains a shorthand for the developmental stage of the specimen, the projectID it belongs to, an X-voxel-count, which provides information on the resolution of the image, a freeform comment for non-HCS-acquisitions and a machineID, which identifies the microscope and the technique the image was acquired with. The projectID again breaks apart into the abbreviated project name, a numeric counter and the abbreviation of the latin species name of the specimen, all separated by hyphens.

- The data-descriptor differentiates between the different stages of processing and analysis of the image. Since all data, which are derived from a given data set carry the same basename (the first three descriptors), the data-descriptor informs the user on the status of modality of the data at hand.

Under individual-image-conditions, file names are constructed interactively with a helper-application, which checks the integrity of the GUID. However, names cannot be assigned directly by the microscope's software and we therefore developed a software tool allowing users to re-establish the association between the experimental history of the sample and its HCI image stack by translating the microscope's file name system into the ZeBraInspector one.

This process is based on a pseudo database system consisting of two spreadsheets (one for input, the other for output) and a couple of javascript and python script. These scripts ensure that the function of the filename as a GUID is not broken by controlling that the right file name components are applied to the correct image and duplications are prevented. The correlation between the image and the underlying sample thereby is established on the basis of the position of the sample in the mounting grid. This information is conveyed in the microscope-generated file name and entered into the input spreadsheet. Careful user guidance on the input spreadsheet facilitates its use and increased user confidence.

wdr12 **mutants**

wdr12^{h}i3120Tg mutants were obtained from the Zebrafish International Resource Center (ZIRC, Eugene, OR, USA). Adult zebrafish were maintained as heterozygotes and inbred to generate homozygous mutant embryos. EE were sorted under a stereomicroscope (Olympus SZX16) on day 5. Nearly 25% of them appeared with eyes smaller than in non-mutant EE of the same developmental stage and were considered *a priori* mutants. Putative mutants and siblings were processed according to the zFaCT protocol. After imaging, all fish were unmounted and subjected *a posteriori* to genotyping. Wildtype and mutant *wdr12* alleles were detected with the following primers: forward 5'-ACCCAGCTGACATTTGCTCT-3', reverse 5'-TTCTTGGCTTCCAGCAGTTT-3' and reverse2 5'-CAATATCACCAGCTGAAGCCTA-3'. PCR using forward and reverse primers yield a 244bp amplicon on the wildtype allele. PCR using forward and reverse2 primers yield a 831bp amplicon on the mutant allele.

bioRxiv preprint doi: https://doi.org/10.1101/2020.10.26.353656; this version posted October 26, 2020. The copyright holder for this preprint (which was not certified by peer review) is the author/funder. All rights reserved. No reuse allowed without permission.

5-FU treatments

5-fluorouracil (Sigma, USA) was applied using DMSO as a carrier. Three types of control conditions were involved : zebrafish in embryo medium, zebrafish in embryo medium placed in six-well plates with 5-FU treated fish, zebrafish in embryo medium+DMSO. 5-FU application protocol is described in the Result section. At 5 dpf, imaging of all EE was first performed under the dissecting microscope. Then mountings using 48-well moulds were performed to allow homogenous acquisitions between samples under our fast confocal microscope. No changes in the microscopy parameters were done between the three successive experiments.

Image treatments and statistical analysis

We performed registration, segmentation, statistical analysis and graph plotting using a python 3.7 environment under Ubuntu 16.04 and Windows 10 in an HP computer with a Intel Core i7 vPro CPU and 32 GB of RAM. We used Numpy, Scipy (Virtanen et al., 2020), scikit Image (van der Walt et al., 2014; Yaniv et al., 2018), matplotlib (Hunter, 2007), openpyxl, Pink (Couprie, 2011) and SimpleITK (Yaniv et al., 2018).

Statistical analysis was performed as follows : A Fisher test was performed to compare variances of the two clusters to be compared. If variances were equal, a student test was performed. Otherwise, a Welch test was performed.

We manually performed 3D segmentations of whole EE and their white matter using Amira for Life & Biomedical Sciences software (Thermo Fisher Scientific, USA). Then, we compared them to their corresponding automatic ones.

To measure segmentation accuracy, we computed Matthews correlation coefficient (MCC), Sørensen-Dice coefficient (DSC) and general balanced metric (Cappabianco et al., 2019) setting $\boldsymbol{\delta}$ = 2 (GB2). DSC and GB2 did not take true negatives into account. This problem is balanced by computation of the MCC. However, the large amount of black voxels around the sample could create computational artifacts. To avoid these artifacts, the computation of MCC is performed in a bounding box around the union of both manual and automatic segmentations with a tolerance of 5 voxels. We add GB2 because this coefficient balanced false positive over false negative. Associated with DSC and MCC, this led to a better estimation of the segmentation accuracy.

Our ZeBrainInspector (ZBI) graphical interface was developed using Pyside2 library. The workspace screen displays up to 6x3 views at the same time. Rotations, slices stacking, section moves and contrast enhancement are computed in real time using Numba library to obtain Python and Numpy code acceleration. Thus, the software was built only using native Python code.

Guidelines to get a user-friendly ZeBraInspector (ZBI) software

For any request, please contact zbi@tefor.net. We will try to answer as shortly as possible.

Help can be found by clicking on **?** in each software page.

bioRxiv preprint doi: https://doi.org/10.1101/2020.10.26.353656; this version posted October 26, 2020. The copyright holder for this preprint (which was not certified by peer review) is the author/funder. All rights reserved. No reuse allowed without permission.

Download software at https://tefor.net/portfolio/zebrainspector, execute it (a security window might appear, click on complementary information and execute). Software launch may last one minute.

Software was developed for zebrafish 5-day zebrafish EE. With time we will validate its use with other stages and other species. Similarly we will try with other types of microscopes. Please keep us informed of your results with other types of tools and samples at zbi@tefor.net!

If needed, also **download images for demos** at https://tefor.net/portfolio/zebrainspector

Screen resolution: software was optimized for 1920x1080 screens. Large screens of course improve rendering.

Image format and depth: only nd2, mha and tif are accepted. Image analysis algorithms were developed on 12 bit unsigned integer-encoded images. These algorithms are not able to work with lower encoding, like 8 bit images. However, they may work properly with higher integer encodings, like 16 bit images.

Image specifications: whole EE needed for registration algorithms, better with head on the left of the image. It is recommended to use a computer with at least 32Go of RAM that will run smoothly with 2500X1000X500 voxel images (voxel size around two microns, voxels must be isotropic). Objective with a field of 0,5 millimeter: 12x2 tiles. Objective with a field of 1 millimeter: 6x1 tiles. Performance increases with RAM: either larger images and/or higher numbers can be loaded in the soft.

Configure interface: numbers of lines and columns to see per page and channels to view. On the right of the top menu bar, select zoom mode: single image, lines, rows or all visible images on the screen. Zoom is performed by clicking on an image.

Contrast of the reference dye channel must be precisely tuned. No specific parameter is needed (more guidelines in the Microscopy chapter before). With depigmented samples, saturate slightly retina layers and check that lens and background have grey levels at zero. For samples with pigmlented eye, check that membrane over the eye is well visible, as deep as possible in the sample.

Downsampling factor. When a file of 2500x1000x500 voxels is loaded, its resolution is downsampled four times by default. The dynamic range for rendering is reduced to 8 bits. Hence, the software loads 100 files of such type in memory with only 2.4Go of RAM requested. Avoiding downsampling (left in the top menu bar) leads to better renderings but might be slow with large numbers of samples. Adapt for best compromise between sample numbers and sizes and rendering quality.

Optical sections H, S and T buttons in top menu bar display respectively horizontal, sagittal and transverse views. Moreover, a rotation around the anteroposterior axis can be performed.

bioRxiv preprint doi: https://doi.org/10.1101/2020.10.26.353656; this version posted October 26, 2020. The copyright holder for this preprint (which was not certified by peer review) is the author/funder. All rights reserved. No reuse allowed without permission.

Visualizations are maximum intensity projections of thick optical sections of the sample around the chosen slice. Size of the section could be selected from 4 to 40 µm.

Snapshot capture. To ease observation of a particular structure or before capture, contrast may be tuned by clicking on CH O 1 2 in the bottom menu bar. Click on the snapshot button below each image. Extraction of image may take one minute. Then save high resolution versions of selected images in a folder (original file name is changed, sample numbers in the current sessions are kept, capture parameters and dates are kept in the file name) .

Segmentation

Segmentation must be performed before registration.

To start segmentation, it is mandatory to select reference/dye channel and output channel. Further computations will be processed on raw data of the dye/reference channel and results will be displayed on the output channel. If the output channel is populated, the segmentation will replace the previous image.

By default, results will be saved in mha. A checkbox offers to save results in tiff instead of mha.

Before processing, the software will ask for a destination folder. Segmentation results will be saved in the chosen folder.

Segmentation performed on a 1Gb image lasts around ten minutes depending on computer hardware.

Registration

To start registration, select reference/dye channel. Like segmentation, further computations will be performed on raw data of the chosen channel. If registrations of segmentations are needed , perform them just after registration or reload segmentation output files with initial raw data.

By default, the software considers that samples were depigmented using H_2O_2 . Then segmentation is performed using lenses, because eye pigments are rendered transparent. For mutants with pigmentation defects, when depigmentation step is not performed to preserve native fluorescence, the “pigmented eyes (no H2O2 treatment)” checkbox should be checked. The registration algorithm will use eye shapes. Like segmentation, a checkbox offers to save results as tiff instead of mha and the software will ask for a destination folder before computation.

For an image containing three channels of 1 Gb, computation may last five minutes per sample depending on computer hardware.

Volumetric analysis results in an excel table A lipophilic dye (DiI ,Dio) stains myelin sheaths of neuron fibers , forming a nervous system domain called white matter. At 5dpf, this staining provides a good overview of brain morphology. EE volume is the number of pixels contained in the segmented EE, which provides a measure of its size (many other measures may be added).

To start volumetric analysis, select images with correct segmentations by checking the “selected” checkbox below each image. Click on the volumetry button in the bottom menu bar. During the

bioRxiv preprint doi: https://doi.org/10.1101/2020.10.26.353656; this version posted October 26, 2020. The copyright holder for this preprint (which was not certified by peer review) is the author/funder. All rights reserved. No reuse allowed without permission.

volumetric analysis, numbers of voxels that are found in each segmentation are counted. Since voxels are 3D elements, these numbers could be extrapolated as volumes. A third value is computed as the ratio of the white matter over the volume of the whole sample. These three values are stored in a spreadsheet to allow further statistical analysis.

Troubleshooting

Software does not start

ZBI was developed to start under Windows or Linux environments. A binary file is available for windows. For linux environment, codes are available in a gitlab repository, and the software could be compiled locally. Running ZBI codes under Mac environments was not tested, and this run is not intended to work properly. The main window of ZBI should be displayed in approximately one minute. If the software does not start, please verify that a C++ compiler is present in the computer. For Windows environments, visual C++ 2017 should be installed.

Software freezes

This software was designed to work with data of 1 Go per channel on a computer with at least 32 Gb. Lower RAM dimensions may not be able to treat this data, inducing a software freeze.

Closing the registration or the segmentation windows will not stop running processes. Please wait for the end of one computation before starting the other one to avoid RAM overload and then software freeze. Navigation in the software is slower during computation.

Registrations fail

Most probably, image is not well taken in charge by algorithms due to low noise/signal ratio for the dye signal, or saturation of the dye signal in too large domains. Insufficient clearing of samples leading signal loss in depth might avoid registration (refer to Lempereur et al., 2020 in MMTA for an algorithm of contrast improvement for confocal images). Please check protocols and guidelines for image acquisition. Obviously, registrations in casper background are often less successful than when lenses are used with depigmented eyes, because eyes, which are used do not have similar sizes, are not spheric and eye boundaries are hardly visible ventrally, because they are hidden during imaging by more dorsally located eye pigments.

Also, strongly deformed EE might not be appropriately recognized by the software.

bioRxiv preprint doi: https://doi.org/10.1101/2020.10.26.353656; this version posted October 26, 2020. The copyright holder for this preprint (which was not certified by peer review) is the author/funder. All rights reserved. No reuse allowed without permission.

Results and discussion

We established the ZeBraInspector (ZBI) platform to perform high content imaging (HCI) and high-content analysis (HCA) of 3D images in the context of zebrafish neurodevelopment. Based on the observation that lipophilic tracers yield intense labeling in the brain, we designed a simple and standardized procedure to stain, mount, image and analyse whole 5dpf EE using these dyes. Stainings allow registrations of the signals, thus allowing a huge gain of time at the mounting step by permitting poor orientations of the samples. The software also performs volumetric estimations of the whole-body and of the brain matter. All steps have been optimized to minimize time and effort for the experiment and promote its portability. Considering a batch of 48 samples, only about eight days are needed for completion from initial fixation to the quantification of the brain and whole EE volumes (Fig. 1).

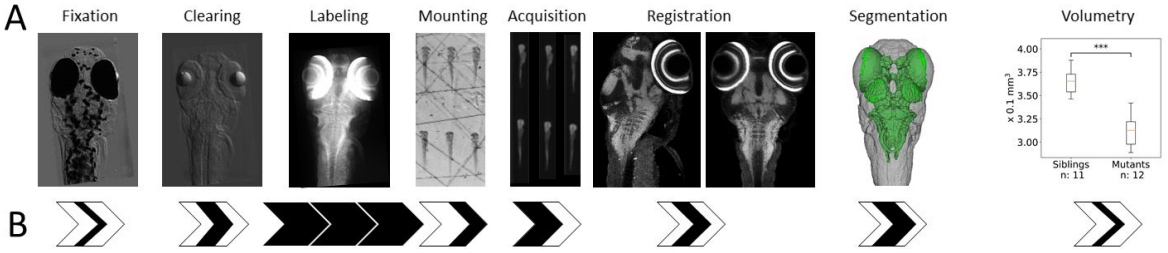

Fig. 1 The ZeBraInspector platform

(A) The ZeBraInspector platform has several steps. After fixation, it starts with a tissue clearing process to reduce light diffusion and absorption, before staining with a lipophilic dye. Samples are mounted using specific moulds for automatic fast mircoscopic acquisitions. Then, acquisitions are registered to simplify selection of samples before segmentation, and speed snapshot captures. To finish, computed segmentations are analyzed to provide volumetric analysis.

(B) Time consumption of each step of ZeBraInspector platform. Each arrow represents a day of treatment. Black sections approximately represent the rate of time needed in one day of experiment. The whole process takes about 10 days from fixation to provide volumetric analysis.

High-content 3D image analysis requires reliable features for automatic segmentation: a robust labeling and tissue clearing protocol

High-content 3D image analysis requires consistent fluorescence signals for automatic segmentation. We tested lipophilic dyes of the carbocyanine family (e.g. DiO, DiI and DiD) to reliably visualize main morphological features of the EE (Fig. 0 and Fig. 2). When applied as a counterstain, which is facilitated by the small size of the EE, this type of dyes - traditionally used for electrode marking and neuronal tracing - strongly stains the membrane rich white matter of the brain. Due to the lower density of membranes in non-neural tissues, the staining was less pronounced than in the brain, but nevertheless sufficient for automatic segmentation of the whole body. We established a staining protocol, which achieved optimal permeabilization while preserving the shape of the EE.

It can be tuned to directly record native fluorescence from reporter lines (Fig. 0B-C), skipping the depigmentation step, provided an unpigmented genetic background is used (Materials and

bioRxiv preprint doi: https://doi.org/10.1101/2020.10.26.353656; this version posted October 26, 2020. The copyright holder for this preprint (which was not certified by peer review) is the author/funder. All rights reserved. No reuse allowed without permission.

Methods). It is scalable with an optional immunolabeling step using anti-GFP/RFP or other antibodies (Fig. 0D-H) if additional morphological data are needed.

Sample clearing is needed for confocal microscopy, because otherwise in 5 dpf zebrafish a slight signal loss is observed with increasing depth. Indeed, homogeneously illuminated images are needed for the subsequent automatic segmentation steps, also along the Z axis of the image stack. Incubation in mild detergents leads to a partial delipidification promoting clearing of the samples. Crucial for the success of the tissue clearing is the imaging buffer, which equalibrates the refractive index (RI) of the sample with that of the surrounding medium, thus rendering cell membranes, cytoplasm proteins and other cell components transparent. After a series of tests of several products and concentrations, we opted for a medium mainly based on sucrose, nicotinamide and triethanolamine (MD+, refer to Materials and Methods section), which has suitable optical parameters for imaging with dipping lens objectives with high or tunable RIs.

Result of DiO labeling of a representative 5 dpf zebrafish is shown in Fig. 2. As shown in Fig. 2A, the DiO displays a homogenous labeling and strongly highlighted areas with a high density of myelinated fibers. Retina photoreceptors, olfactory bulbs and main fibers tracts of the brain display a very strong DiO signal and allow detection of fine anatomical structures and landmarks (Fig. 2 E-H: telencephalon, optic commissures, lateral forebrain bundle, optic tectum, medial longitudinal fascicle). Moreover, all anatomical structures are labeled. Outside the brain, ganglions and motoneurons (Fig. 2A), appearing as dots along the spinal cord, are strongly positive. Muscles (Fig. 2A) and other non-neuronal structures (Fig. 2C: yolk, digestive tract and organs, etc...) display low DiO fluorescence signal compared to brain structures but remain detected. Overall these data show that DiO can be used as a marker of brain structures and used to detect whole-EE, using background labeling.

bioRxiv preprint doi: https://doi.org/10.1101/2020.10.26.353656; this version posted October 26, 2020. The copyright holder for this preprint (which was not certified by peer review) is the author/funder. All rights reserved. No reuse allowed without permission.

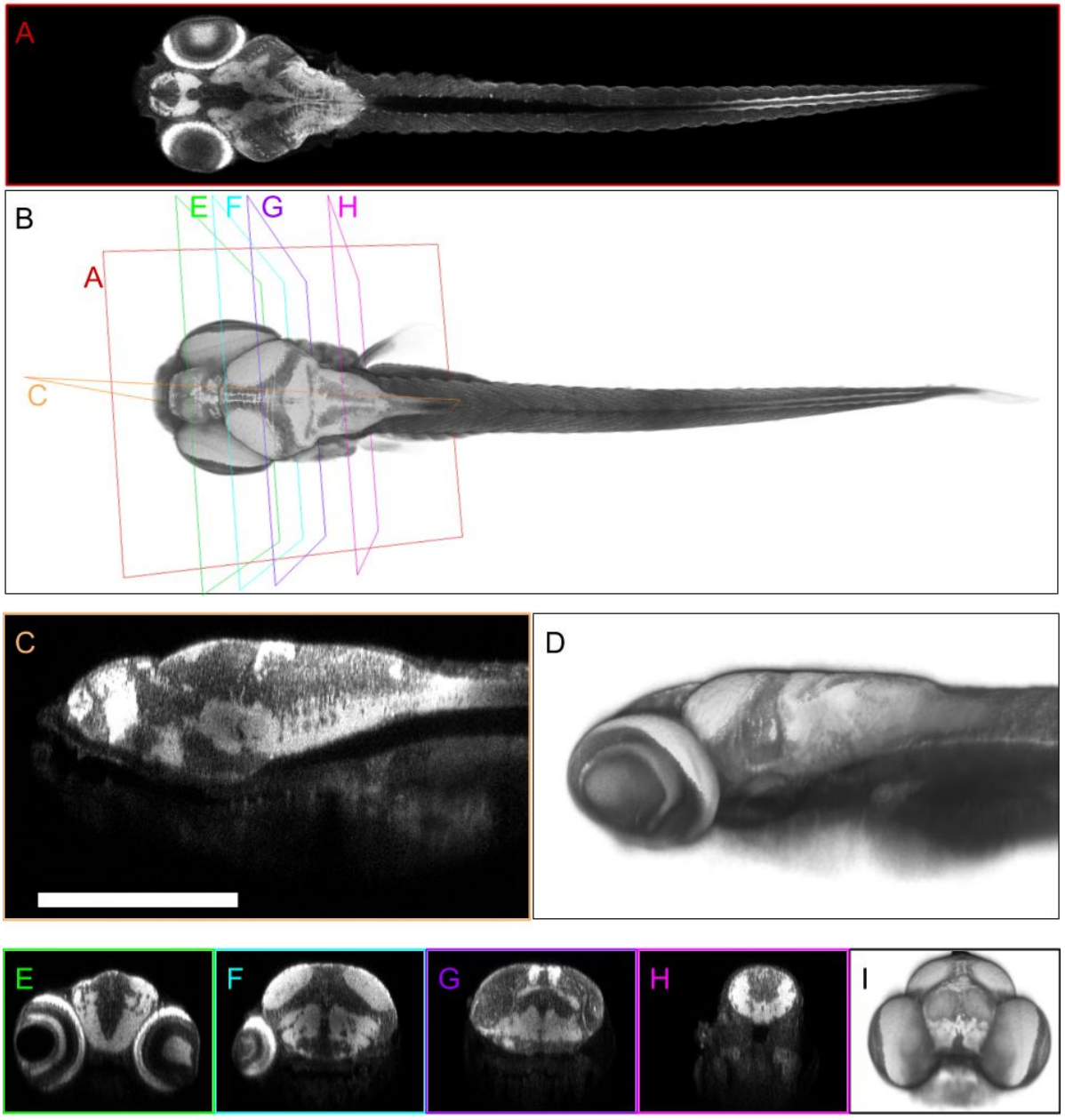

Fig. 2 The lipophilic dye DiO: a reliable marker for the visualization of brain white matter and whole EE.

Five dpf zebrafish were labeled with the lipophilic DiO marker and cleared in high-RI medium (RI 1,457). Five fields of view are stitched together for acquiring whole-EE with a 10X multi-immersion objective with RI correction ring. (A, C, E-H) Two-micron-optical sections (raw data) from the confocal microscope shown in Fig. 3. Section planes are shown in B. B, D, I: 3D volume rendering of the EE (raw data). (A) Horizontal section, plane of imaging. (B) Dorsal view. (C) Sagittal section (posterior region cropped). (D) Lateral view of EE anterior region. (E-H) Transverse sections. (I) Frontal view of the EE head.

bioRxiv preprint doi: https://doi.org/10.1101/2020.10.26.353656; this version posted October 26, 2020. The copyright holder for this preprint (which was not certified by peer review) is the author/funder. All rights reserved. No reuse allowed without permission.

HCI on hundreds of samples : a description of a set-up to fastly mount EE

Many mounting strategies for high-throughput microscopy of zebrafish EE have been published (Alessandri et al., 2017; Donoughe et al., 2018; Kleinhans and Lecaudey, 2019; Staal et al., 2018; Westhoff et al., 2013; Wittbrodt et al., 2014) but most of them are adapted to embryos and not to 5dpf EE. Motivated by the work of the Recher group (Alessandri et al., 2017), we designed 3D printed fixtures for the generation of regular grids of small niches of approximately the shape and size of our samples. Hence, one placed into these narrow niches by means of fine paintbrushes, EEs remain in this position. This mounting strategy is allowed by the fact that EE in high RI medium do not dessicate as fastly as if they were in water. EE are immobilized with a drop of phytagel, a transparent plant culture medium (Zhou et al., 2019) which serendipitously proved to be ideal for microscopy. EE can be placed with the dorsal or ventral side up, depending on the region of the brain to analyze. One of the efficient features of our platform is that no perfect EE orientation is needed, provided a too dorsally located eye does not perturb acquisition of the brain region found below the eye. Imaging plates and stamps are chosen adapted to the number of samples .

HCI requires speed : a description of the main advantages of fast confocal laser scanning microscopy

Although being the most powerful method for live applications, we did not select light-sheet microscopy. Indeed, although their diversity has offered easier image acquisitions, many require a high degree of optical and informatics expertises that may not be available to many experimental biology groups (Albert-Smet et al., 2019). With such microscopes, mounting of zebrafish EE in agarose at large-scale is difficult, and may require sophisticated robotics, especially because of the side illumination, which precludes simply using plates as with upright microscopes. Also image artifacts result from side illumination (stripes, shadows) or unequal thickness of the light sheet. With the idea of combining high throughput, portability and high resolution 3D imaging, we devised a fast confocal laser scanning microscope (CLSM) equipped with commercially available devices. Confocal microscopes are available in most imaging facilities. They are user-friendly and present less risks of image acquisition failures or artifacts. They generate reasonable data sizes. Depth dependent loss of signal is a recurrent criticism against confocal microscopy. Tissue clearing techniques and the algorithms we use in this study to correct signal loss with depth overcome this drawback.

Our setup (described in detail in the Materials and Methods section) is based on a Nikon A1R HD upright microscope equipped with a piezo-electric objective scanning nanofocusing system allowing high-speed Z movements over a range of 2 mm, together with a fast x/y motorized stage. Increasing movement speeds is highly efficient to shorten acquisition times. Another crucial parameter is the use of a low magnification high numerical aperture multi-immersion objective allowing imaging of large fields (1200 1200 µm) with expected resolution for analysis at cellular scale (Fig. 3). In these conditions, only five tiles are required to image a single whole zebrafish with cellular resolution in six minutes. We considered a sampling rate of 512X512 voxel as a good compromise between resolution of the tile stack and acquisition time as well as final data size. Overall our imaging parameters allowed us to image one specimen in six minutes and result in a final data file of approximately 1-1.5GB. Finally, to improve the speed of image acquisition, the

bioRxiv preprint doi: https://doi.org/10.1101/2020.10.26.353656; this version posted October 26, 2020. The copyright holder for this preprint (which was not certified by peer review) is the author/funder. All rights reserved. No reuse allowed without permission.

microscope also comprises a high definition resonant scanner coupled with two high-sensitivity photo-multiplicators.

bioRxiv preprint doi: https://doi.org/10.1101/2020.10.26.353656; this version posted October 26, 2020. The copyright holder for this preprint (which was not certified by peer review) is the author/funder. All rights reserved. No reuse allowed without permission.

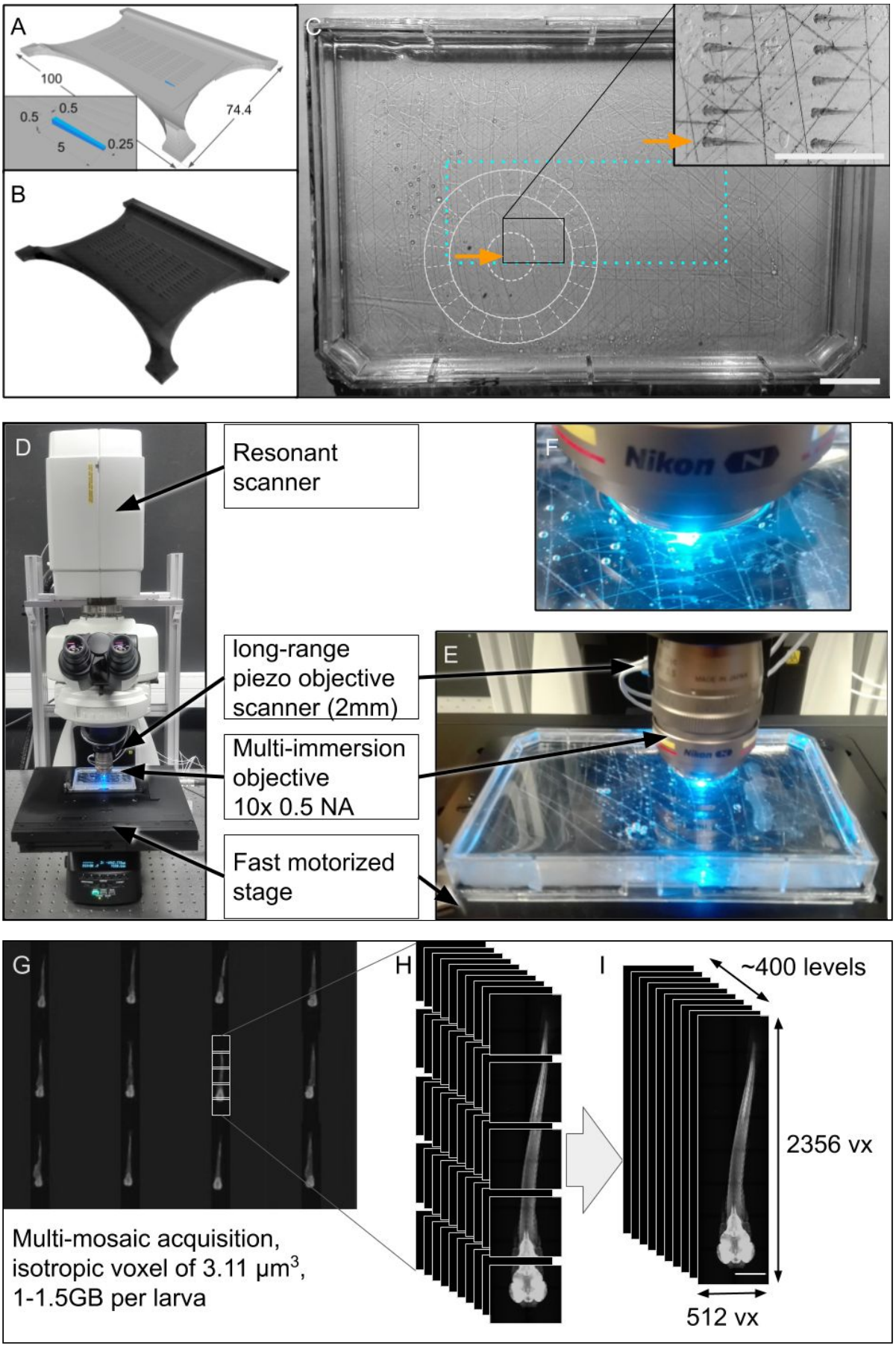

bioRxiv preprint doi: https://doi.org/10.1101/2020.10.26.353656; this version posted October 26, 2020. The copyright holder for this preprint (which was not certified by peer review) is the author/funder. All rights reserved. No reuse allowed without permission.

Fig. 3 HCI tools and strategy.

(A) Modelling the stamp in CAD-software. All measurements in millimeters. (B) 3D-printed plastic stamp. (C) Dissecting microscope view of a single-well-plate with 48 embedded samples. The round, light-grey line diagram represents the microscope objective; this demonstrates why there is so much space needed between the rim of the single-well plate and the specimens. The cyan dotted rectangle outlines the overall scan-area. The grey lines are manually applied scratches in the plastic of the plate to reinforce the adhesion of the agarose to the dish. Scale bar: 5mm. (D) overview on the CLSM setup. (E) focus on the dipping lens and the long-range piezo objective scanner. (F) high-magnification view of the imaging setup displaying grid of embedded fish (21 dpf) (G) Partial screenshot of the Nikon acquisition software (NIS-element) displaying a multi-mosaic acquisition of 12 samples. (H) Mosaic-acquisition: since the specimen is bigger than the field of view, multiple tile-stacks with 10% overlap are acquired independently. These data are recorded with a sampling rate of 512X512 voxels (vx) of 2.5X2.5 µm . With a correspondingly adjusted z-step size this results in isotropic voxels. (I) Dimensions of a standard data set. The resulting image-stack after merging of the tile-stacks contains about 400 slices, each 512 vx wide and 2256 vx long.

bioRxiv preprint doi: https://doi.org/10.1101/2020.10.26.353656; this version posted October 26, 2020. The copyright holder for this preprint (which was not certified by peer review) is the author/funder. All rights reserved. No reuse allowed without permission.

HCA of whole-EE and their brain white matter

Presentation of the pipeline

To be able to analyze the important amount of acquired data, we developed a software to automate as much as possible the analysis (Fig. 4). The first step is a renaming tool to get file names informative for the user. Then, in the frame of the ZeBraInspector (ZBI) softwarer, registration allows to simplify comparisons between samples. Maximum intensity projections of substacks of the image can be generated. This allows the removal of invalide samples before segmentation to reduce computational time. These segmentations will automatically detect positions of the EE and its white matter in the original acquisition. However, segmentation errors could occur. To remove these errors, a new visualization is offered to the user. It will display the segmentations compared to raw data. After removal of incorrect segmentations, ZBI computes volumetric analysis.

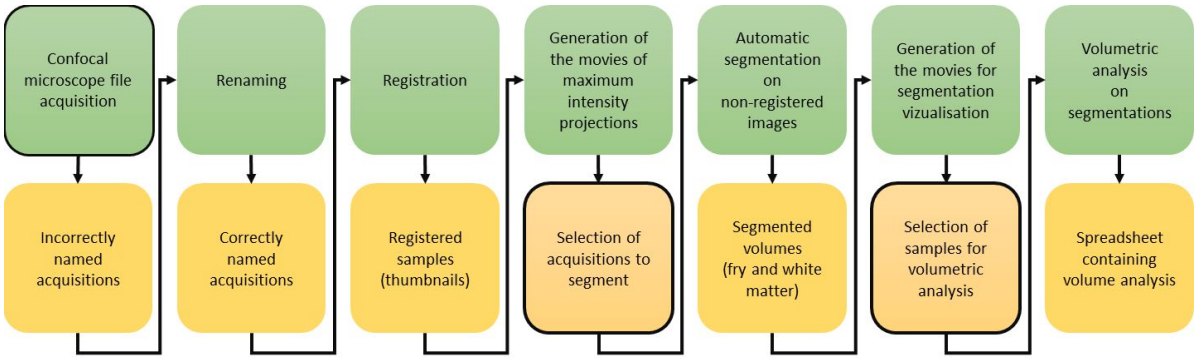

Fig. 4 The ZeBraInspector informatic pipeline allows to register, segment and visualize high-content 3D images

ZBI pipeline consists of a succession of computation steps. The acquired datasets are renamed, registered and segmented. Segmentations are used to perform volumetric analysis. Framed squares represent sequences that need user manipulations.

Guidelines for high-content images (HCI)

In our pipeline, our microscope's software generates image stacks by merging individual tiles. However, in other contexts, stitching procedure may be performed by user prior image treatment. It is recommended to perform stitching by previously reconstructing volumes from each image tile and then computes 3D stitching.

bioRxiv preprint doi: https://doi.org/10.1101/2020.10.26.353656; this version posted October 26, 2020. The copyright holder for this preprint (which was not certified by peer review) is the author/funder. All rights reserved. No reuse allowed without permission.

Different image sizes can be processed by our algorithm. Image processing is performed using voxels as a standard unit of measurement. Isotropic voxels are recommended.

We encourage recording images with 12-bit depth to get a good representation of the dynamic range of the datasets in the digitized data. A correctly acquired image should have an equilibrated gray value histogram. All the gray values allowed by the 12-bit encoding should be used while limiting saturation. If the image uses only a portion of the gray value range, histogram equalization may be used.

In addition, it is important to maximize the contrast within the image. For dye acquisition, the laser power should be chosen so as to saturate only the photoreceptor layer of the retina, limiting the saturation of other tissues to a minimum. In addition, it is preferable that the background noise outside the sample be as low as possible. Thus, the choice of offset should limit the number of non-zero voxels outside the sample.

Images must be saved in a format that allows for the preservation of metadata. The nd2 and mha formats are capable of preserving this information and are compatible with the ZBI software. Sample tracking through the different phases of the experiment represents an important goal, which requires a solid data management plan. To maintain flexibility in the choice of analytic tools and accessibility to a wide variety of users, we developed a data management system which is entirely based on structured file names (Material and Methods).

Registration for faster EE visualization in batch

In order to facilitate the comparison between samples, a procedure for registering the samples has been implemented. The original image (Fig. 5A,E) is morphologically closed, and then morphologically opened to smooth the signal. This smoothed image is then thresholded to keep the highest ten percent of gray values. A rough segmentation of the white matter is thus obtained by keeping the biggest element of this thresholding result (Fig. 5B,F). A vector describing the main orientation of the white matter is defined retaining the largest half axis (major semi-axis) of the ellipse encompassing the thresholded voxels. To reduce computation time for further steps, the original image is downsampled to a quarter of its original size in each dimension. A rough segmentation of the whole larva is computed by thresholding the downsampled image, keeping the biggest element of the thresholding result, then performing a closing and finally removing internal holes. To detect black elements into the specimen, a watershed is computed using first the five lower percents of gray values as interior markers, then outside of the larva and highest fifty percent of gray values as external markers and finally a morphological gradient of the closed image as the topological map. Among the dark elements, lenses are detected by keeping the two largest spherical elements (Fig. 5 B,F). These two landmarks thus make it possible to obtain two vectors : the interocular vector, from the center of one crystalline lens to the other, and the translation vector, pointing from the center of the lenses to the center of the whole image. To ensure orthogonality, the vector describing the main axis of the white matter is projected on the plane defined by the interocular one. A last vector is obtained by calculating the vector product between the interocular vector and the projected vector. This forth vector is oriented to point to the part of the image with the highest average gray value. The four vectors (Fig. 5 C,G) are then used to calculate the transformation matrix used to align the image with its axis (Fig. 5 D,H). The calculation

bioRxiv preprint doi: https://doi.org/10.1101/2020.10.26.353656; this version posted October 26, 2020. The copyright holder for this preprint (which was not certified by peer review) is the author/funder. All rights reserved. No reuse allowed without permission.

of the translation and rotation matrices on the DiO channel allows to apply this image registration to all signals acquired in parallel to the DiO reference channel.

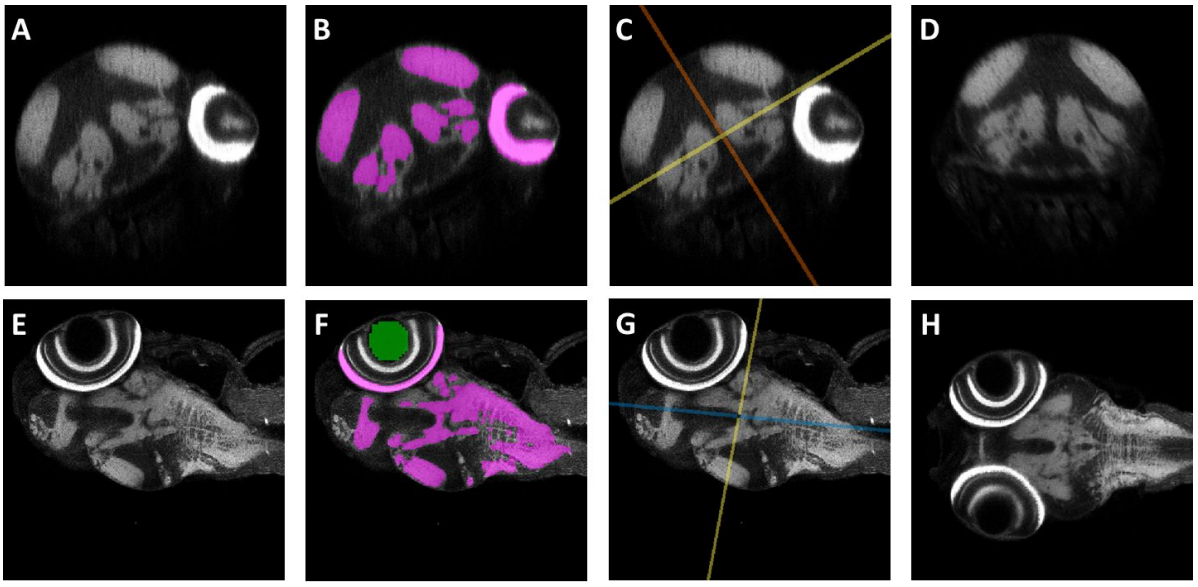

Fig. 5 A registration method using lens as landmarks and brain white matter fitting ellipsoid for EE axis definition

(A-D) Midbrain dorsal sections. (E-H) Midbrain transverse section (A,E) Raw data. (B, F) Superpositions of segmentation of the whitte matter (magenta) and crystalline lenses (green) to the raw data (gray). These landmarks are used to compute the direction of the white matter. (C, G) Superposition of orientation planes to raw data (grey). Yellow, blue and red lines represent lens to lens, main axis and third axis planes respectively. (D,H) Results of the registration. The sample is centered and the white matter is aligned to the main axis of the image.

Segmentation of the whole EE

A central task of our processing pipeline is the segmentation of the whole EE. To achieve automatic segmentation that flexibly adapts to images that always exhibit slight intensity and quality diversity, whatever the efforts for standardization are made, many steps are required. First, a morphological closing that eliminates local under-segmentations due to local gradients is followed by a morphological opening eliminating background noise external to the sample. This smoothed image is first used to calculate a morphological gradient, which reflects the transitions of gray values in the image. Where an abrupt transition occurs, white pixels are visible, while homogenous regions appear in dark. This draws a topological map as an intermediate result. Then, two thresholds based on gray levels of the smoothed image are applied: the level of the first threshold corresponds to the internal zones (body) of the sample by keeping the high values and the second corresponds to the external zones (background) by keeping the low values. Using these thresholds, we labeled the local maxima of the smoothed image by assigning them a value of 0, 1 or 2 depending on the area where they are located. 0, 1 and 2 are respectively neutral, external and internal seeds.

bioRxiv preprint doi: https://doi.org/10.1101/2020.10.26.353656; this version posted October 26, 2020. The copyright holder for this preprint (which was not certified by peer review) is the author/funder. All rights reserved. No reuse allowed without permission.

The next step consists of a segmentation based on the watershed method which requires seeds and a topological map. Seeds, which correspond to the values 1 or 2 defined above, will serve as initialization for the watershed. Thus, during the watershed procedure, these seeds will grow to fill the area of interest. The algorithm is first applied to a subsampled version of the image in order to know the position of the sample. Hence, when the high resolution image is processed, this allows to limit the computation of the watershed to the sample, thereby reducing the calculation time. However, due to remaining light diffusion into tissues, the acquisition side is brighter than the opposite side. To solve this problem and improve segmentation accuracy, a specific threshold is computed on the acquisition side to remove low grey values. Finally, a morphological closure is applied to eliminate potential non-segmented areas inside of the EE.

In order to validate this segmentation method, we imaged twelve samples using the corresponding grid and computed segmentations using our pipeline (Fig. 6A). Following segmentation, the results were controlled using ZBI and this led us to discard two weakly labeled samples resulting in abnormal segmentations. We compared the automatic segmentations (Fig. 6B-E) to manual segmentations (Fig. 6F-I). We obtained median Sorensen-Dice coefficient, general balanced metric (GB2) and Matthew correlation coefficient (MCC) values around 0.95 (Fig. 6J). These high scores indicated correspondence between the manual and automatic segmentations. The time required to calculate an automatic segmentation is on average six minutes, similar to the eight minutes needed for acquisition. This calculation time, estimated on standard laptops, could certainly be reduced by paralleling the calculations on dedicated computation servers. In conclusion, our automatic segmentation method automatically achieves precise segmentation of the whole EE.

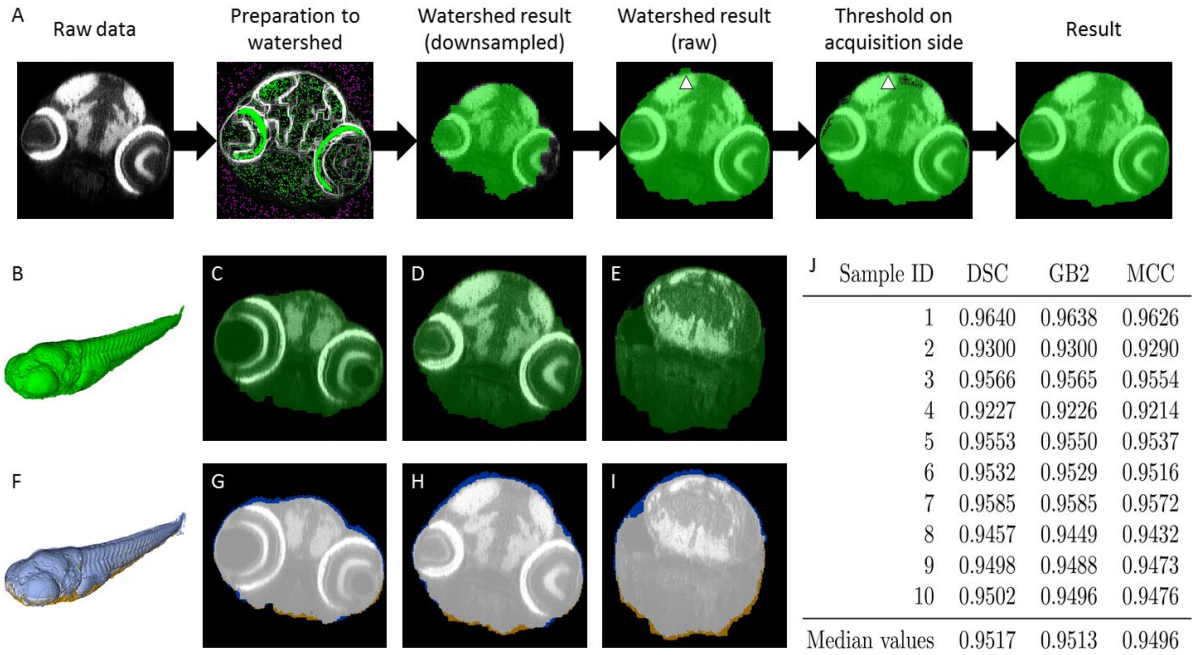

Sample ID	DSC	GB2	MCC
1	0.9640	0.9638	0.9626
2	0.9300	0.9300	0.9290
3	0.9566	0.9565	0.9554
4	0.9227	0.9226	0.9214
5	0.9553	0.9550	0.9537
6	0.9532	0.9529	0.9516
7	0.9585	0.9585	0.9572
8	0.9457	0.9449	0.9432
9	0.9498	0.9488	0.9473
10	0.9502	0.9496	0.9476
Median values	0.9517	0.9513	0.9496

Fig. 6 Pipeline and validation of segmentation of the EE

(A) Main steps of the computation of the EE segmentation performed by watershed. Each step is illustrated using a transverse section of the midbrain. Due to light scattering, the acquisition side is brighter than the opposite size. Then, the watershed over-segments dorsally (arrowheads). This problem is solved by applying a specific threshold on the acquisition side. Algorithms are available in gitlab (refer to Materials and Methods). (B-E) Results of segmentation. Segmentation in green, raw data in grey. B. 3D surface rendering. C-E. Transverse section.(F-I) Comparison of manual and

bioRxiv preprint doi: https://doi.org/10.1101/2020.10.26.353656; this version posted October 26, 2020. The copyright holder for this preprint (which was not certified by peer review) is the author/funder. All rights reserved. No reuse allowed without permission.

automatic segmentations. Raw data in grey. Manual segmentation only, automatic segmentation only and intersection between both are respectively in brown, blue and white. F. 3D surface rendering. (G-I) Transverse section. (J) MCC, GB2 and SDC coefficients for automatic segmentations compared to manual segmentations. Median values of these coefficients are around 0.95, indicating that the two strategies of segmentations lead to almost identical results.

Brain white matter segmentations

We exploited the property of DiO to strongly mark the white matter of the brain to achieve an automatic segmentation of this tissue. As for the segmentation of the whole EE, the first step consists in calculating a morphological opening followed by a closing. These steps generate a smoothed image, used to calculate a first threshold keeping the 10% of the brightest gray values in the image. This thresholding creates a class of voxels that we consider to be part of white matter. A second thresholding is performed on the smoothed image in order to preserve the 50% of the lowest gray values of the image. To improve the precision of the segmentation by watershed, we perform an erosion of the thresholding results in order to ensure the presence of a neutral range between the two zones obtained. As in the previous chapter, we then keep the local maxima of the smoothed image within each zone to create an image including the necessary seeds for watershed.

The presence of elements strongly marked by DiO outside the brain, for example within the digestive tract, requires a second step to refine the segmentation to the brain. We only select the largest segmented element, corresponding to the brain. We then calculate a morphological expansion of this object, in order to create the root allowing the calculation of a geodesic expansion using the result of the watershed as a mask. This step removes elements that are not part of the brain while retaining small isolated brain structures.

Using a similar strategy than in the previous chapter to validate the segmentation, we segmented the brain white matter of the previous ten EE (Fig. 7). Comparisons between automatic and manual segmentations (Fig. 7F-I) revealed median DSC, GB2, and MCC values of around 0.88 (Fig. 7J). Automatic segmentation took an average of additional 3 minutes. Hence whole body and brain white matter segmentations are performed in a time comparable to that of image acquisition.

bioRxiv preprint doi: https://doi.org/10.1101/2020.10.26.353656; this version posted October 26, 2020. The copyright holder for this preprint (which was not certified by peer review) is the author/funder. All rights reserved. No reuse allowed without permission.

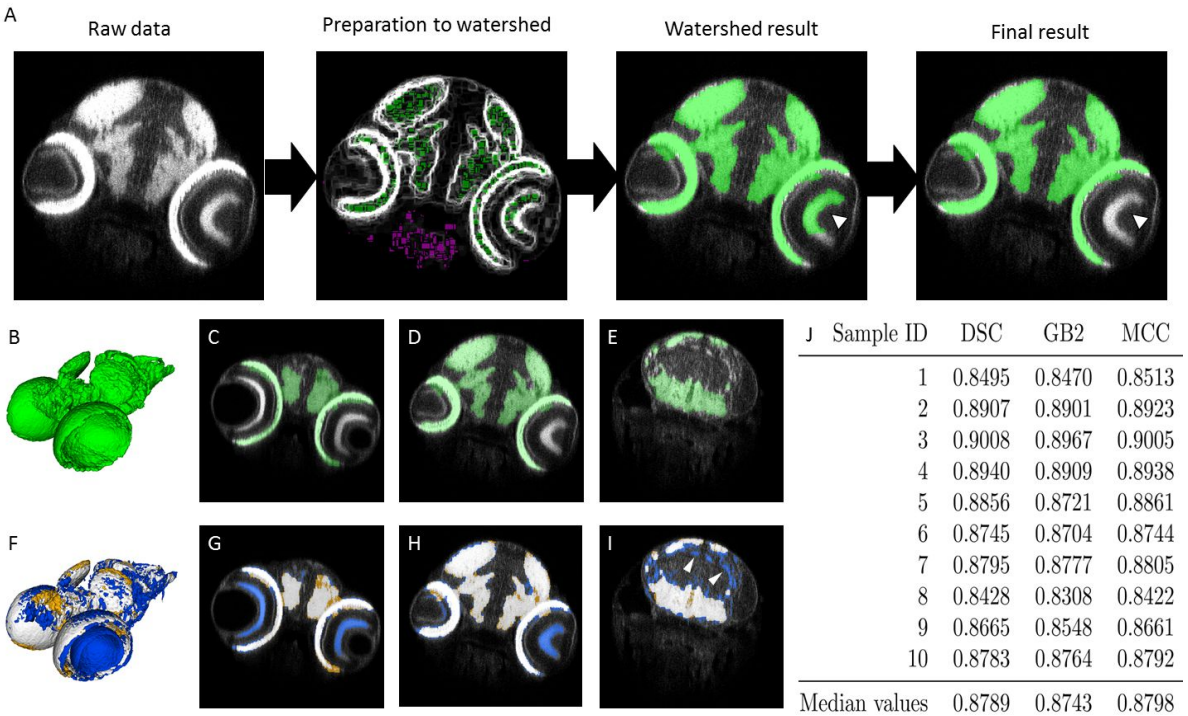

J

Sample ID	DSC	GB2	MCC
1	0.8495	0.8470	0.8513
2	0.8907	0.8901	0.8923
3	0.9008	0.8967	0.9005
4	0.8940	0.8909	0.8938
5	0.8856	0.8721	0.8861
6	0.8745	0.8704	0.8744
7	0.8795	0.8777	0.8805
8	0.8428	0.8308	0.8422
9	0.8665	0.8548	0.8661
10	0.8783	0.8764	0.8792
Median values	0.8789	0.8743	0.8798

Fig. 7 Pipeline and validation of segmentation of the white matter

(A) Main steps of the computation of the white matter segmentation performed by watershed. Each step is illustrated using a transverse section of the midbrain. Watershed computation detects unwanted elements, like retina (arrowHead) or yolk (not show). These oversegmentations are removed by selection of the biggest elements and its close neighboors. Details of the process are available in gitlab (refer to Materials and Methods). (B-E) Results of segmentation. Segmentation in green, raw data in grey. (B) 3D surface rendering. (C-E) Transverse section. (F-I) Comparison of manual and automatic segmentations. Raw data in grey. Manual segmentation only, automatic segmentation only and intersection between both are respectively in brown, blue and white. (F) 3D surface rendering. (G-I) Transverse section. (J) MCC, GB2 and SDC coefficients for automatic segmentation compared to manual segmentations. Coefficients are superior to 0.8 indicating that automatic segmentations are precise enough to perform further volumetric analysis. Indeed, segmentation errors are similar in all samples. For example, small white matter tracts in the brain are not segmented (arrowheads in I).

Segmentation accuracy control by the user

In order to allow users to interactively control the quality of the segmentations, the software produces an image superimposing the segmentation of the white matter on the segmentation of the whole EE. Via ITK-SNAP or any other viewer allowing navigation in 3D images, it is then possible to compare these segmentations with raw data. Furthermore, this superimposition of segmentations allows the automatic creation of movies that show the overlay of the segmentation on the raw data, for example in transverse sections. These movies can be used to detect potential segmentation errors, and remove some samples before starting statistical analyses.

bioRxiv preprint doi: https://doi.org/10.1101/2020.10.26.353656; this version posted October 26, 2020. The copyright holder for this preprint (which was not certified by peer review) is the author/funder. All rights reserved. No reuse allowed without permission.

Moreover, our software generates superimposition of the thumbnails generated at the initial step of the pipeline with the segmentation of the selected section. This allows the detection of failed segmentation. The software proposes to eliminate them prior to launching statistical analyses.

Volumetric analysis

In order to obtain volumetric analyses, the number of segmented voxels in each segmented specimen is multiplied by the physical voxel size. This yields its real-world volume. Using both segmentations, this computation will give two different volumes: the whole EE volume and the volume of its white matter. Dividing the volume of the white matter by the volume of the EE, we obtain a ratio that may inform about a more subtle defect in neural development such as a decreased neurogenesis. These values are then automatically saved in an excel sheet and returned to the user.

HCA by the ZeBraInspector (ZBI) platform reveals discrete but statistically significant brain defects

A very large collection of mutants is now available in zebrafish. More than 500 are annotated in the Zfin database as having brain development defects (Davis et al., 2014). In most cases, phenotyping is performed using a dissecting microscope or the annotations are extracted from the literature. In this section, we describe the use of our pipeline to refine the characterization of a microphthalmic mutation in a ribosome biogenesis gene. We selected the *Wdr12* mutant line in which visible eye microphthalmia was reported in lateral transmission light microscopy pictures (two and six dpf) at the Zfin database (Fig. 9A). We performed crosses of heterozygous founders and selected approximately one-fourth of 5 dpf EE based on the microphthalmia criteria. We first confirmed on one batch of EE that the affected EE were homozygous for the mutation (data not shown). Eye phenotypes were therefore 100% penetrant in *wdr12* homozygous (Hmz) embryos, while heterozygous (Htz) embryos were indistinguishable from wild-type (Wt) siblings.

We tested if brain hypomorphy could be detected in *wdr 12* mutants using our HCA analysis. It did not appear obvious in our initial observations under the dissecting microscope and was not annotated in the microscope pictures available in the Zfin database. This was surprising since in most of these mutants, eyes, brain and other tissues are globally hypomorphic, due to global decrease in cell proliferation (Brombin et al., 2015; Brooks et al., 2014). At 5dpf, we euthanized, fixed and stained the experimental animals and acquired 3D image stacks (as described in the Method section) of the lipophilic dye labels(Fi.g 8B-C). We launched our algorithms on 12 Wt/Htz EE and 12 Hmz mutant EE to estimate EE and brain white matter volumes.

To extract maximum intensity projections of transversal thick sections of the midbrain, we used the ZeBraInspector (ZBI) platform (Fig. 8, refer to Methods for details on the protocol and guidelines), which has the advantage to allow navigation in parallel in registered samples, hence greatly speeding the extraction of images at appropriate levels. ZBI allows the visualization of both raw data and segmentation results thus providing a quick and efficient way to analyze images in batches.

bioRxiv preprint doi: https://doi.org/10.1101/2020.10.26.353656; this version posted October 26, 2020. The copyright holder for this preprint (which was not certified by peer review) is the author/funder. All rights reserved. No reuse allowed without permission.

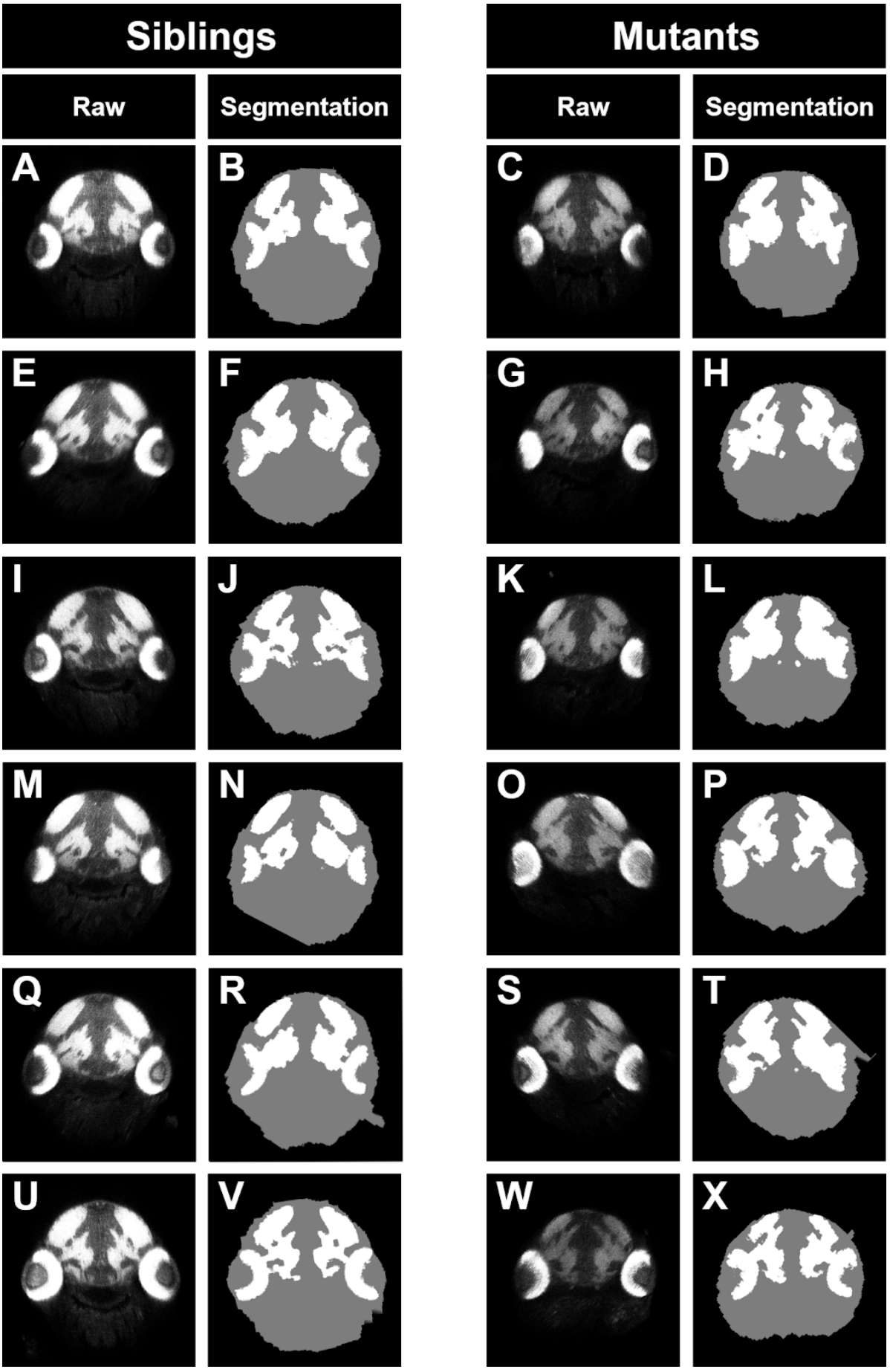

bioRxiv preprint doi: https://doi.org/10.1101/2020.10.26.353656; this version posted October 26, 2020. The copyright holder for this preprint (which was not certified by peer review) is the author/funder. All rights reserved. No reuse allowed without permission.

Fig. 8 Use of the ZebraFishInspector (ZBI) platform to study the morphology of midbrains of *wdr12* mutants

The twelve samples shown illustrate the homogeneity of brain sizes in mutants and in wild types.

A slight hypomorphy of whole-body (gray disk) and brain white matter (in white) can be observed in the mutants (C, G, K, O, S, W) when compared to siblings (A, E, I, M, Q, U). Nevertheless the quantitative results obtained by the volumetric analysis from 3D images (Fig. 10) reveals much more striking statistically significant differences of body and brain white matter size between mutants and siblings, hence illustrating the advantage of using 3D images. Volumetric analysis allowing statistical tests is performed on segmentation results (B, D, F, H, J, L, N, P, R, T, V, X). Segmentation algorithm accuracy is demonstrated in this figure.

This volumetric analysis first clearly revealed that mutants are overall smaller than their Wt/Htz siblings (Fig. 9G; Welch test: p=5.10-08), confirming the overall growth deficits observed in these mutants. In addition, although the white matter volume was strongly inferior in mutants (Welch test, p=3.10-06) (Fig. 9H), we found no relative decrease in the volume of the white matter compared to global EE volume in these mutants (Fig. 9I), strongly suggesting that this mutation affected brain growth but that the decrease in brain white matter volume was not more dramatic in this organ than in others, and rather correlated with overall dwarfism. Visual analysis of registered images revealed normal morphology of the brain.

bioRxiv preprint doi: https://doi.org/10.1101/2020.10.26.353656; this version posted October 26, 2020. The copyright holder for this preprint (which was not certified by peer review) is the author/funder. All rights reserved. No reuse allowed without permission.

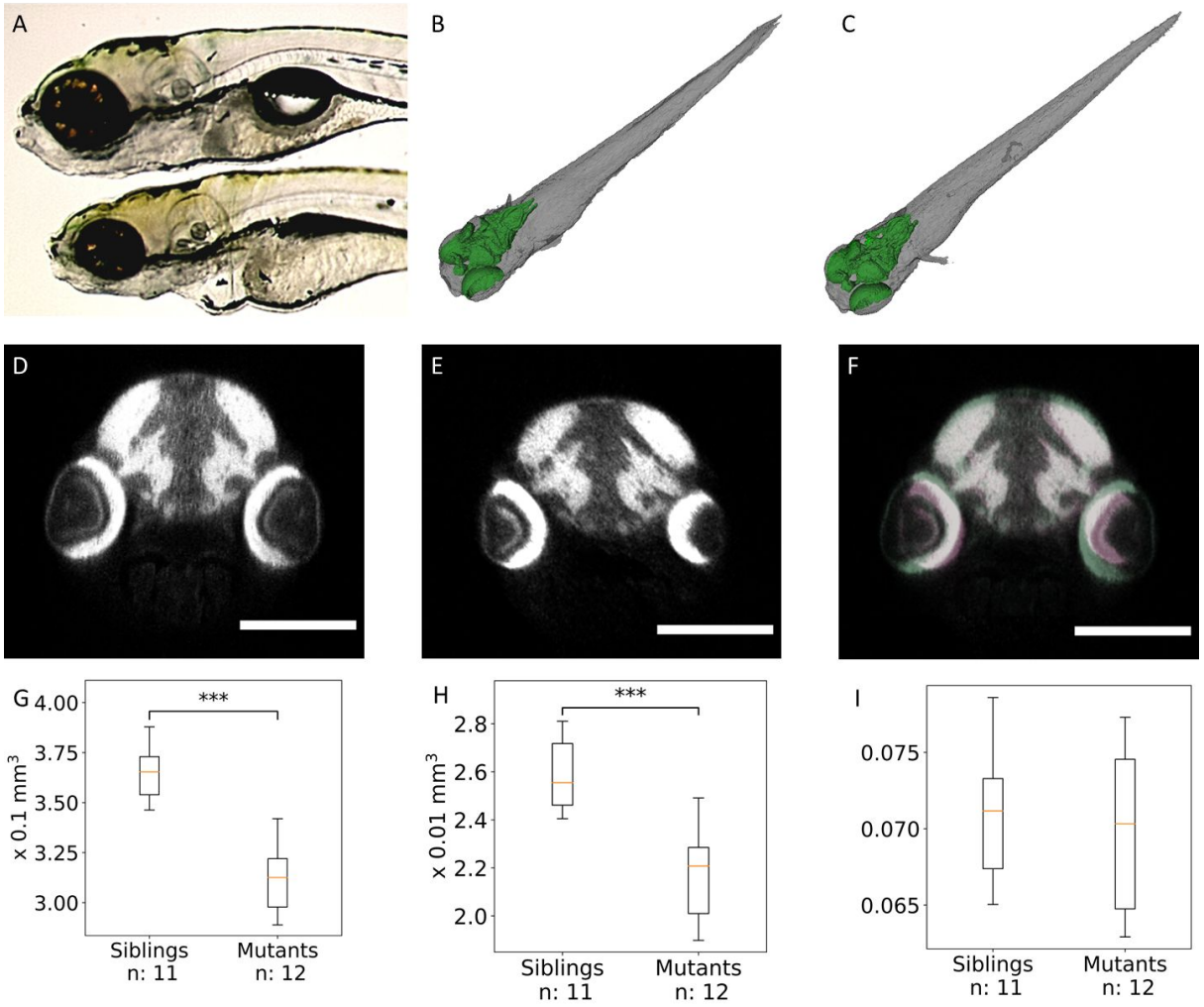

Fig. 9 Volumetric analysis of white matter and whole body in Wdr12 Mutants reveals a statistically significant global hypomorphy

(A) Widefield microscopy of six dpf EE. Wild-type on top, *wdr12*$^{hi3120Tg/hi3120Tg}$ mutants below. Eyes are smaller but it is not possible to phenotype whether mutant and sibling brain sizes are different. (B-C) 3D surface rendering of segmentations. EE in grey, white matter in green. These visualizations do not allow to illustrate any obvious difference between mutants and siblings. (B) WT or Htz mutants (C) Hmz Mutants. (D-E) Transverse sections. Mutants have obviously smaller eyes but these 2D pictures do not allow to distinguish mutant brain phenotype from sibling one. (G-I) Boxplots of whole EE volumes(G), brain volumes (H) and brain over EE volume ratios (I). Mutants are significantly smaller than siblings. Also brain volume is significantly decreased in mutants. However, EE and brain volume decreases are homothetic indicating that the brain, as other tissues, is hypomorphic in this ribosome biogenesis mutant probably following slowered cell proliferation.

This study illustrates the power of our approach to detect and confirm with only twelve samples discrete but significatively smaller volumes of the EE, and of the brain, not visible nor reported before. Fast volumetric analysis succeeded to produce statistically significant results with only twelve 3D images (Fig. 9G-H). Therefore identification of brain volume defects in eight mutants

bioRxiv preprint doi: https://doi.org/10.1101/2020.10.26.353656; this version posted October 26, 2020. The copyright holder for this preprint (which was not certified by peer review) is the author/funder. All rights reserved. No reuse allowed without permission.

may be performed by imaging only two dishes containing 48 samples. This proposed method paves the route to other refined analyses involving other brain markers or other organs.

HCA to assess the effect of early developmental exposure to environmentally relevant concentrations of 5-fluorouracil

To estimate the performance of the ZeBraInspector platform for large scale HCI in toxicology, we performed 5-fluorouracyl (5-FU) treatments on batches of 48 samples.

Six batches of fifteen recently spawned eggs were randomly placed in six well plates. In one of the wells, control fish were placed in embryo medium/DMSO to test if any toxicity may be due to a passage by air of the 5-FU. Additionally, two other control conditions were included in each experiment (embryo medium alone, and embryo medium/DMSO). Active concentrations of 5-FU were determined from (Kovács et al., 2016), and correspond to approximately one million times the concentrations found in the environment (Kosjek et al., 2013) and 2 to 40 times times the concentrations found in plasma of human receiving colon cancer treatments (Casale et al., 2004). For all treatments, EE were chronically exposed to 5-FU for five days, beginning from one hour post-fertilization, by changing medium each day. Each day, mortality was recorded and dead fish removed with no significant difference between conditions (not shown) .

All specimens appeared indistinguishable from controls (Fig. 10A) under the dissecting microscope. Only 20% of EE exposed to 2g/l exhibited obvious abnormalities: shortened body axis and head, microphtalmia, cardiac oedema, abnormal swim bladder and shortened yolk vesicle (Fig. 10B).
We randomly kept six samples for HCI. We performed the experiment in triplicate. No significant difference was observed between these triplicates so we pooled fish treated with same concentrations for the volumetric analysis. We first measured EE volume using our pipeline (Fig. 10I). EE in the highest 5-FU concentrations were significantly smaller. This is in contrast with previous reports surprisingly mentioning increased fish sizes due to 5-FU treatments (Kovács et al., 2016) . We suggest that these contradicting results might be mainly due to the time point when the compound is applied. While in (Ng et al., 2020) treatments were initiated at 5dpf, we indeed paid attention to start treatments less than one hour after spawning, occurring at the beginning of the light-phase of the circadian rhythm. We anticipated that this would allow the best entry of 5-FU into the chorion. Indeed the perivitelline space still grows up to 1 hpf due to osmotic water inflow and the chorion hardens and becomes more impermeable at later stages. This hypothesis was confirmed by experiments involving treatment initiations later post-fertilization (>6h), which did not induce any defects even at high doses (data not shown).

Our analysis showed a significant decrease in the volume of the brain white-matter (Fig. 10J), more accentuated than the whole EE volume (Fig. 10I) as shown by the ratio between white matter and EE volumes (Fig. 10K). Interestingly, this decrease was not obvious on transverse sections (Fig. 10C-H). Using 3D images, we were thus able to detect discrete defects. Moreover, careful observations of DiO patterns suggested slightly disorganized white-matter for example in the pretectum (Fig. 10I-K).

bioRxiv preprint doi: https://doi.org/10.1101/2020.10.26.353656; this version posted October 26, 2020. The copyright holder for this preprint (which was not certified by peer review) is the author/funder. All rights reserved. No reuse allowed without permission.

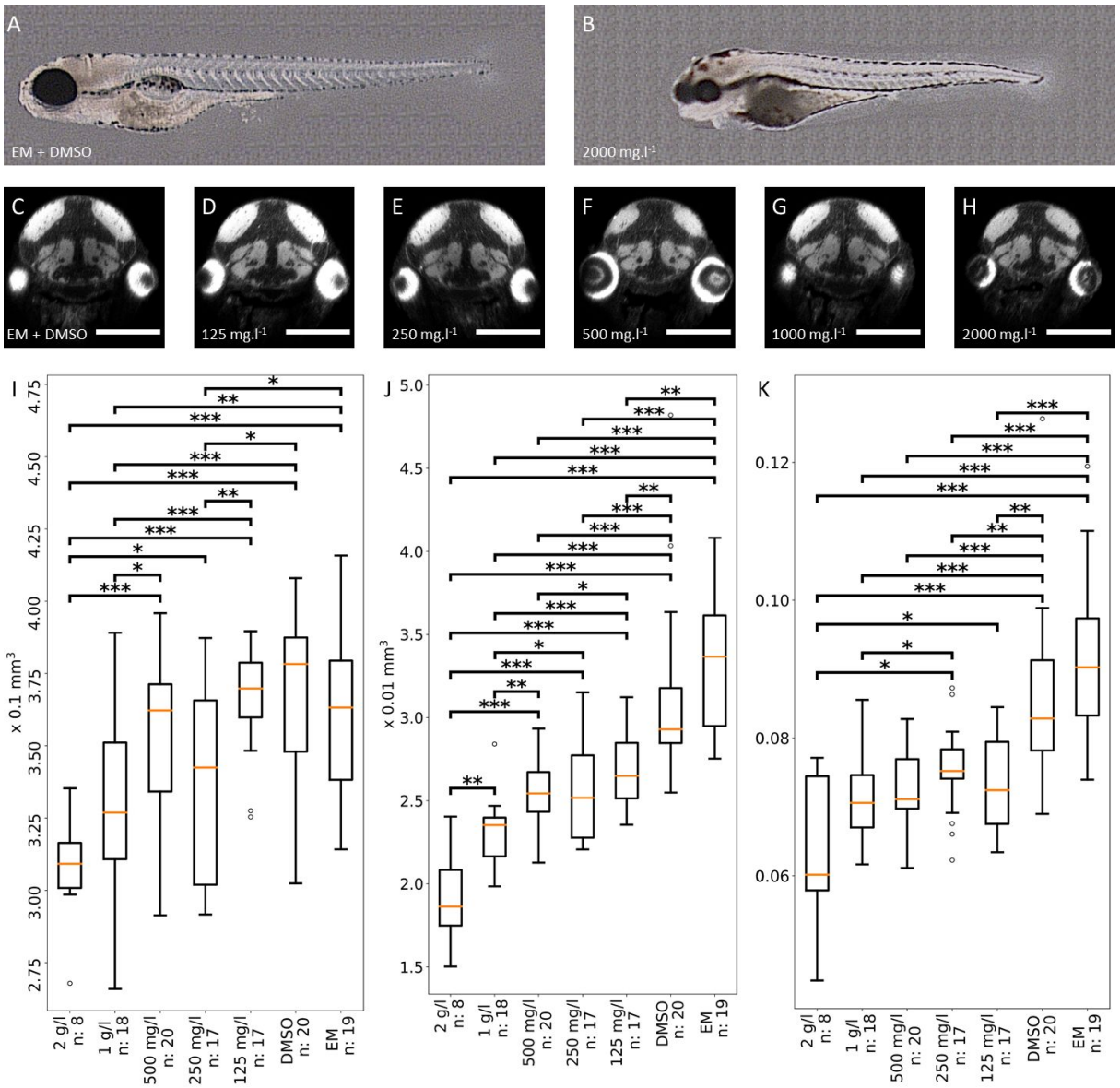

Fig. 10 Medically relevant concentrations of 5-FU lead to dwarfism and microcephaly

(A) Dissecting microscope side view of a control EE. (B) Corresponding side view of a EE treated by 2g/l of 5-FU exhibiting short body axis, cardiac oedema, and diverse abnormalities. (C-H) Transverse 2D sections through midbrains of control zebrafish or fish exposed to 5-FU appear similar. Identical levels of section plans in the brain were selected. However, due to variations in the orientations of sections eyes are not always sectioned at the same level. (AC Control EE exposed to DMSO. (D-H) EE exposed to 125, 250 , 500, 1000 and 2000 mg/l, respectively. Scale bar = 250 µm(G-L) (I-K) Boxplots of whole EE volumes. (I), brain volumes (J) and brain over EE volume ratios (K). EE treated with high concentrations of 5-FU are significantly smaller than controls. Their brains are also significantly smaller. Moreover, white matter/whole EE volume ratios indicate that brains have a significantly more decreased size than EE indicating that 5-FU might specifically affect neurogenesis leading to strong microcephaly.

bioRxiv preprint doi: https://doi.org/10.1101/2020.10.26.353656; this version posted October 26, 2020. The copyright holder for this preprint (which was not certified by peer review) is the author/funder. All rights reserved. No reuse allowed without permission.

Overall, our platform reveals that early developmental exposure of zebrafish embryos to medically-relevant concentrations of 5-FU affects growth and brain white-matter size, as expected from an antiproliferative agent. With a single dish containing 48 samples, the ZeBraInspector platform allowed an accurate estimation of toxic dose ranges. This constituted a basis to study the fine morphological changes associated with behavioral defects, following the comparison of morphological screens and behavioral screens.

Conclusion Perspectives

We developed a fast and flexible high-resolution 3D image acquisition and analysis platform for HCI on 5 dpf EE, named ZeBrainInspector. While the basic volumetric analysis of this pipeline can be performed on the basis of a simple lipophilic dye labelling, more specialized phenotypes can be investigated by integrating immunohistochemical labelling against the appropriate epitopes or employing transgenic lines which are expressing a fluorophore in the [region/tissue] of interest. Standardized breeding, staining, mounting and imaging techniques provide the consistent quality and high number of 3D images required for a statistical analysis on population-level. As a convenient way of interacting with the automated volumetric analysis a graphical user interface allows the user to revise the data quality and sample population on the basis of preprocessed, lightweight representations of the raw data. This interface also can be used for the analysis of highly variable phenotypes in zebrafish mutants. For example it can be used to sort samples with various levels of defects and then analyze patterns of a transgene-expression or antibody-labelling more reliably.

The modular nature of our processing pipeline allows the integration of additional analysis modules, which can be developed specifically for a given application. Currently active developments of further analysis modules are focused on the integration of machine learning to accelerate the process of image segmentation for volumetry and non-rigid registration to increase the sensitivity of detection of volumetrically neutral deformations within the sample. For bigger studies we foresee an increase of productivity by further robotorization of the specimen-handling during mounting and image acquisition, consequent usage of 96-well plates and - as far as the studies in question permit - a reduction of the sampling rate.

This pipeline was tested on studies of subtle volumetric aberrations in transgenic mutants as well as the neurodevelopmental impact of an ecotoxic compound and can be modified and scaled to any HCE application, which needs to investigate the impact of test-compounds on an entire, physiologically intact vertebrate model organism, on a holistic level.

bioRxiv preprint doi: https://doi.org/10.1101/2020.10.26.353656; this version posted October 26, 2020. The copyright holder for this preprint (which was not certified by peer review) is the author/funder. All rights reserved. No reuse allowed without permission.

Bibliography

Affaticati, P., Simion, M., De Job, E., Rivière, L., Hermel, J.-M., Machado, E., Joly, J.-S., Jenett, A., 2017. zPACT: Tissue Clearing and Immunohistochemistry on Juvenile Zebrafish Brain. Bio Protoc 7. doi:10.21769/BioProtoc.2636

Albert-Smet, I., Marcos-Vidal, A., Vaquero, J.J., Desco, M., Muñoz-Barrutia, A., Ripoll, J., 2019. Applications of Light-Sheet Microscopy in Microdevices. Front. Neuroanat. 13, 1. doi:10.3389/fnana.2019.00001

Alessandri, K., Andrique, L., Feyeux, M., Bikfalvi, A., Nassoy, P., Recher, G., 2017. All-in-one 3D printed microscopy chamber for multidimensional imaging, the UniverSlide. Sci. Rep. 7, 42378. doi:10.1038/srep42378

Aleström, P., D'Angelo, L., Midtlyng, P.J., Schorderet, D.F., Schulte-Merker, S., Sohm, F., Warner, S., 2019. Zebrafish: Housing and husbandry recommendations. Lab. Anim. 23677219869037. doi:10.1177/0023677219869037

Beaumont, K.A., Anfosso, A., Ahmed, F., Weninger, W., Haass, N.K., 2015. Imaging- and Flow Cytometry-based Analysis of Cell Position and the Cell Cycle in 3D Melanoma Spheroids. J. Vis. Exp. e53486. doi:10.3791/53486

Brombin, A., Joly, J.-S., Jamen, F., 2015. New tricks for an old dog: ribosome biogenesis contributes to stem cell homeostasis. Curr. Opin. Genet. Dev. 34, 61–70. doi:10.1016/j.gde.2015.07.006

Brooks, S.S., Wall, A.L., Golzio, C., Reid, D.W., Kondyles, A., Willer, J.R., Botti, C., Nicchitta, C.V., Katsanis, N., Davis, E.E., 2014. A novel ribosomopathy caused by dysfunction of RPL10 disrupts neurodevelopment and causes X-linked microcephaly in humans. Genetics 198, 723–733. doi:10.1534/genetics.114.168211

Bruneel, B., Witten, P.E., 2015. Power and challenges of using zebrafish as a model for skeletal tissue imaging. Connect. Tissue Res. 56, 161–173. doi:10.3109/03008207.2015.1013193

Buitrago Santanilla, A., Regalado, E.L., Pereira, T., Shevlin, M., Bateman, K., Campeau, L.-C., Schneeweis, J., Berritt, S., Shi, Z.-C., Nantermet, P., Liu, Y., Helmy, R., Welch, C.J., Vachal, P., Davies, I.W., Cernak, T., Dreher, S.D., 2015. Organic chemistry. Nanomole-scale high-throughput chemistry for the synthesis of complex molecules. Science 347, 49–53. doi:10.1126/science.1259203

Cappabianco, F.A.M., Ribeiro, P.F.O., de Miranda, P.A.V., Udupa, J.K., 2019. A General and Balanced Region-Based Metric for Evaluating Medical Image Segmentation Algorithms, in: 2019 IEEE International Conference on Image Processing (ICIP). Presented at the 2019 IEEE International Conference on Image Processing (ICIP), IEEE, pp. 1525–1529. doi:10.1109/ICIP.2019.8803083

Casale, F., Canaparo, R., Serpe, L., Muntoni, E., Pepa, C.D., Costa, M., Mairone, L., Zara, G.P., Fornari, G., Eandi, M., 2004. Plasma concentrations of 5-fluorouracil and its metabolites in colon cancer patients. Pharmacol. Res. 50, 173–179. doi:10.1016/j.phrs.2004.01.006

Cernak, T., Gesmundo, N.J., Dykstra, K., Yu, Y., Wu, Z., Shi, Z.-C., Vachal, P., Sperbeck, D., He, S., Murphy, B.A., Sonatore, L., Williams, S., Madeira, M., Verras, A., Reiter, M., Lee, C.H., Cuff, J., Sherer, E.C., Kuethe, J., Goble, S., Dreher, S.D., 2017. Microscale High-Throughput Experimentation as an Enabling Technology in Drug Discovery: Application in the Discovery of (Piperidinyl)pyridinyl-1H-benzimidazole Diacylglycerol Acyltransferase 1 Inhibitors. J. Med. Chem. 60, 3594–3605. doi:10.1021/acs.jmedchem.6b01543

Cornet, C., Calzolari, S., Miñana-Prieto, R., Dyballa, S., van Doornmalen, E., Rutjes, H., Savy, T., D'Amico, D., Terriente, J., 2017. Zeglobaltox: an innovative approach to address organ drug

bioRxiv preprint doi: https://doi.org/10.1101/2020.10.26.353656; this version posted October 26, 2020. The copyright holder for this preprint (which was not certified by peer review) is the author/funder. All rights reserved. No reuse allowed without permission.

toxicity using zebrafish. Int. J. Mol. Sci. 18. doi:10.3390/ijms18040864

Couprie, M., 2011. PINK image processing library. Presented at the European Python Scientific Conference.

Davis, E.E., Frangakis, S., Katsanis, N., 2014. Interpreting human genetic variation with in vivo zebrafish assays. Biochim. Biophys. Acta 1842, 1960–1970. doi:10.1016/j.bbadis.2014.05.024

Donoughe, S., Kim, C., Extavour, C.G., 2018. High-throughput live-imaging of embryos in microwell arrays using a modular specimen mounting system. Biol. Open 7. doi:10.1242/bio.031260

Early, J.J., Cole, K.L., Williamson, J.M., Swire, M., Kamadurai, H., Muskavitch, M., Lyons, D.A., 2018. An automated high-resolution in vivo screen in zebrafish to identify chemical regulators of myelination. elife 7. doi:10.7554/eLife.35136

Guo, Y., Veneman, W.J., Spaink, H.P., Verbeek, F.J., 2017. Three-dimensional reconstruction and measurements of zebrafish larvae from high-throughput axial-view in vivo imaging. Biomed. Opt. Express 8, 2611–2634. doi:10.1364/BOE.8.002611

Halder, M., Léonard, M., Iguchi, T., Oris, J.T., Ryder, K., Belanger, S.E., Braunbeck, T.A., Embry, M.R., Whale, G., Norberg-King, T., Lillicrap, A., 2010. Regulatory aspects on the use of fish embryos in environmental toxicology. Integr. Environ. Assess. Manag. 6, 484–491. doi:10.1002/ieam.48

Hunter, J.D., 2007. Matplotlib: A 2D Graphics Environment. Comput. Sci. Eng. 9, 90–95. doi:10.1109/MCSE.2007.55

Jarque, S., Fetter, E., Veneman, W.J., Spaink, H.P., Peravali, R., Strähle, U., Scholz, S., 2018. An automated screening method for detecting compounds with goitrogenic activity using transgenic zebrafish embryos. PLoS ONE 13, e0203087. doi:10.1371/journal.pone.0203087

Kintel, M., Wolf, C., 2020. OpenSCAD, The Programmers Solid 3D CAD Modeller [WWW Document]. URL https://www.openscad.org/ (accessed 6.11.20).

Kleinhans, D.S., Lecaudey, V., 2019. Standardized mounting method of (zebrafish) embryos using a 3D-printed stamp for high-content, semi-automated confocal imaging. BMC Biotechnol. 19, 68. doi:10.1186/s12896-019-0558-y

Kosjek, T., Perko, S., Žigon, D., Heath, E., 2013. Fluorouracil in the environment: analysis, occurrence, degradation and transformation. J. Chromatogr. A 1290, 62–72. doi:10.1016/j.chroma.2013.03.046

Kovács, R., Bakos, K., Urbányi, B., Kövesi, J., Gazsi, G., Csepeli, A., Appl, Á.J., Bencsik, D., Csenki, Z., Horváth, Á., 2016. Acute and sub-chronic toxicity of four cytostatic drugs in zebrafish. Environ. Sci. Pollut. Res. Int. 23, 14718–14729. doi:10.1007/s11356-015-5036-z

Lempereur, S., Jenett, A., Machado, E., Arganda-Carreras, I., Simion, M., Affaticati, P., Joly, J.-S., Talbot, H., 2020. Automated segmentation of thick confocal microscopy 3D images for the measurement of white matter volumes in zebrafish brains. Mathematical Morphology - Theory and Applications 4, 31–45. doi:10.1515/mathm-2020-0100

Ng, M., DeCicco-Skinner, K., Connaughton, V.P., 2020. Using zebrafish to assess the effect of chronic, early developmental exposure to environmentally relevant concentrations of 5-fluorouracil and leucovorin. Environ. Toxicol. Pharmacol. 76, 103356. doi:10.1016/j.etap.2020.103356

Planchart, A., Mattingly, C.J., Allen, D., Ceger, P., Casey, W., Hinton, D., Kanungo, J., Kullman, S.W., Tal, T., Bondesson, M., Burgess, S.M., Sullivan, C., Kim, C., Behl, M., Padilla, S., Reif, D.M., Tanguay, R.L., Hamm, J., 2016. Advancing toxicology research using in vivo high throughput toxicology with small fish models. ALTEX 33, 435–452. doi:10.14573/altex.1601281

Pulak, R., 2016. Tools for automating the imaging of zebrafish larvae. Methods 96, 118–126. doi:10.1016/j.ymeth.2015.11.021

bioRxiv preprint doi: https://doi.org/10.1101/2020.10.26.353656; this version posted October 26, 2020. The copyright holder for this preprint (which was not certified by peer review) is the author/funder. All rights reserved. No reuse allowed without permission.

Roper, C., Tanguay, R.L., 2018. Zebrafish as a model for developmental biology and toxicology, in: Handbook of Developmental Neurotoxicology. Elsevier, pp. 143–151. doi:10.1016/B978-0-12-809405-1.00012-2

Staal, Y.C.M., Meijer, J., van der Kris, R.J.C., de Bruijn, A.C., Boersma, A.Y., Gremmer, E.R., Zwart, E.P., Beekhof, P.K., Slob, W., van der Ven, L.T.M., 2018. Head skeleton malformations in zebrafish (Danio rerio) to assess adverse effects of mixtures of compounds. Arch. Toxicol. 92, 3549–3564. doi:10.1007/s00204-018-2320-y

Susaki, E.A., Tainaka, K., Perrin, D., Kishino, F., Tawara, T., Watanabe, T.M., Yokoyama, C., Onoe, H., Eguchi, M., Yamaguchi, S., Abe, T., Kiyonari, H., Shimizu, Y., Miyawaki, A., Yokota, H., Ueda, H.R., 2014. Whole-brain imaging with single-cell resolution using chemical cocktails and computational analysis. Cell 157, 726–739. doi:10.1016/j.cell.2014.03.042

Susaki, E.A., Tainaka, K., Perrin, D., Yukinaga, H., Kuno, A., Ueda, H.R., 2015. Advanced CUBIC protocols for whole-brain and whole-body clearing and imaging. Nat. Protoc. 10, 1709–1727. doi:10.1038/nprot.2015.085

Tainaka, K., Murakami, T.C., Susaki, E.A., Shimizu, C., Saito, R., Takahashi, K., Hayashi-Takagi, A., Sekiya, H., Arima, Y., Nojima, S., Ikemura, M., Ushiku, T., Shimizu, Y., Murakami, M., Tanaka, K.F., Iino, M., Kasai, H., Sasaoka, T., Kobayashi, K., Miyazono, K., Ueda, H.R., 2018. Chemical landscape for tissue clearing based on hydrophilic reagents. Cell Rep. 24, 2196-2210.e9. doi:10.1016/j.celrep.2018.07.056

van der Walt, S., Schönberger, J.L., Nunez-Iglesias, J., Boulogne, F., Warner, J.D., Yager, N., Gouillart, E., Yu, T., scikit-image contributors, 2014. scikit-image: image processing in Python. PeerJ 2, e453. doi:10.7717/peerj.453

Virtanen, P., Gommers, R., Oliphant, T.E., Haberland, M., Reddy, T., Cournapeau, D., Burovski, E., Peterson, P., Weckesser, W., Bright, J., van der Walt, S.J., Brett, M., Wilson, J., Millman, K.J., Mayorov, N., Nelson, A.R.J., Jones, E., Kern, R., Larson, E., Carey, C.J., SciPy 1.0 Contributors, 2020. SciPy 1.0: fundamental algorithms for scientific computing in Python. Nat. Methods 17, 261–272. doi:10.1038/s41592-019-0686-2

Westhoff, J.H., Giselbrecht, S., Schmidts, M., Schindler, S., Beales, P.L., Tönshoff, B., Liebel, U., Gehrig, J., 2013. Development of an automated imaging pipeline for the analysis of the zebrafish larval kidney. PLoS ONE 8, e82137. doi:10.1371/journal.pone.0082137

Wittbrodt, J.N., Liebel, U., Gehrig, J., 2014. Generation of orientation tools for automated zebrafish screening assays using desktop 3D printing. BMC Biotechnol. 14, 36. doi:10.1186/1472-6750-14-36

Xiaoqin Tang, van't Hoff, M., Hoogenboom, J., Yuanhao Guo, Fuyu Cai, Lamers, G., Verbeek, F., 2016. Fluorescence and bright-field 3D image fusion based on sinogram unification for optical projection tomography, in: 2016 IEEE International Conference on Bioinformatics and Biomedicine (BIBM). Presented at the 2016 IEEE International Conference on Bioinformatics and Biomedicine (BIBM), IEEE, pp. 403–410. doi:10.1109/BIBM.2016.7822552

Yaniv, Z., Lowekamp, B.C., Johnson, H.J., Beare, R., 2018. SimpleITK Image-Analysis Notebooks: a Collaborative Environment for Education and Reproducible Research. J. Digit. Imaging 31, 290–303. doi:10.1007/s10278-017-0037-8

Zhou, Y., Yan, J., Xu, B.Y., Wang, B.C., 2019. The study on mechanical properties of Phytagel medium. IOP Conf. Ser.: Earth Environ. Sci. 346, 012089. doi:10.1088/1755-1315/346/1/012089